

# Modeling and analysis of a flexible spinning Euler-Bernoulli beam with centrifugal stiffening and softening: A Linear Fractional Representation approach with application to spinning spacecraft

R. Rodrigues<sup>a,\*</sup>, D. Alazard<sup>a,1</sup>, F. Sanfedino<sup>a,2</sup>, T. Mauriello<sup>a,3</sup>, P. Iannelli<sup>a,4</sup>

<sup>a</sup>*Institut Supérieur de l'Aéronautique et de l'Espace (ISAE-SUPAERO), Université de Toulouse, 10 Avenue Edouard Belin, BP-54032, 31055, Toulouse Cedex 4, France*

---

## Abstract

The derivation of a linear fractional representation (LFR) model for a flexible, spinning and uniform Euler-Bernoulli beam is accomplished using the Lagrange technique, fully capturing the centrifugal force generated by the spinning motion and accounting for its dependence on the angular velocity. This six degrees of freedom (DOF) model accounts for the behavior of deflection in the moving body frame, encompassing the bending, traction and torsion dynamics. The model is also designed to be compliant with the Two-Input-Two-Output Port (TITOP) approach, which offers the possibility to model complex multibody mechanical systems, while keeping the uncertain nature of the plant and condensing all the possible mechanical configurations in a single LFR. To evaluate the effectiveness of the model, various scenarios are considered and their results are tabulated. These scenarios include uniform beams with fixed root boundary conditions for different values of tip mass, root offset and angular velocity. The results from the analysis of the uniform cantilever beam are compared with solutions found in the literature and obtained from a commercial finite element software. Ultimately, this paper presents a multibody model for a spinning spacecraft mission scenario. A comprehensive analysis of the system dynamics is conducted, providing insights into the behavior of the spacecraft under spinning conditions.

**Keywords:** Rotating Cantilever Beams, Centrifugal Stiffening, Flexible Structures, Multibody Dynamics, Spinning Satellites

---

## Nomenclature

AMDM	Adomian Modified Decomposition Method
AMM	Assumed Modes Method
AOCS	Attitude and Orbital Control System
CMS	Component Mode Synthesis
DCM	Direct Cosine Matrix
DOF	Degrees Of Freedom
FEM	Finite Element Method
GNC	Guidance, Navigation and Control

---

\*Corresponding author; Ph.D. student.

*Email addresses:* [ricardo.rodrigues@isae-supaero.fr](mailto:ricardo.rodrigues@isae-supaero.fr) (R. Rodrigues), [daniel.alazard@isae-supaero.fr](mailto:daniel.alazard@isae-supaero.fr) (D. Alazard), [francesco.sanfedino@isae-supaero.fr](mailto:francesco.sanfedino@isae-supaero.fr) (F. Sanfedino), [tommaso.mauriello@student.isae-supaero.fr](mailto:tommaso.mauriello@student.isae-supaero.fr) (T. Mauriello), [paolo.iannelli2@isae-supaero.fr](mailto:paolo.iannelli2@isae-supaero.fr) (P. Iannelli)

<sup>1</sup>Professor

<sup>2</sup>Associate Professor

<sup>3</sup>MSc Student

<sup>4</sup>Postdoctoral Researcher

LFR	Linear Fractional Representation
LPV	Linear Parameter-Varying
SDTlib	Satellite Dynamics Toolbox library
THOR	Turbulence Heating Observer
TITOP	Two-Input Two-Output Ports
TMM	Transfer Matrix Method
3D	Three-Dimensional
$\mathbf{a}_P^{\mathcal{B}} \equiv \left. \frac{d\mathbf{v}_P^{\mathcal{B}}}{dt} \right _{\mathcal{R}_i}$	Inertial linear acceleration vector of the body $\mathcal{B}$ at the point $P$ , expressed in $\text{m s}^{-2}$ .
$\mathbf{v}_P^{\mathcal{B}} \equiv \left. \frac{d\mathbf{x}_P^{\mathcal{B}}}{dt} \right _{\mathcal{R}_b}$	Linear acceleration vector of the body $\mathcal{B}$ computed at the point $P$ with respect to the body frame $\mathcal{R}_b$ , expressed in $\text{m s}^{-2}$ .
$\dot{\boldsymbol{\omega}}_P^{\mathcal{B}}$	Inertial angular acceleration vector of the body $\mathcal{B}$ at the point $P$ , expressed in $\text{rad s}^{-2}$ .
$\mathbf{v}_P^{\mathcal{B}} \equiv \left. \frac{d\mathbf{x}_P^{\mathcal{B}}}{dt} \right _{\mathcal{R}_i}$	Inertial velocity vector of the body $\mathcal{B}$ at the point $P$ , expressed in $\text{m s}^{-1}$ .
$\boldsymbol{\omega}_P^{\mathcal{B}}$	Inertial angular velocity vector of the body $\mathcal{B}$ at the point $P$ , expressed in $\text{rad s}^{-1}$ .
<b>BP</b>	Distance vector defined between the points $B$ and $P$ , expressed in m.
$\mathbf{x}_P^{\mathcal{B}} \equiv \mathbf{OP}$	Distance vector defined between the point $O$ , the origin of the inertial frame, and the point $P$ of the body $\mathcal{B}$ , expressed in m.
<b>BP</b>	Distance vector defined between the points $B$ and $P$ , expressed in m.
$\boldsymbol{\Theta}_P^{\mathcal{B}}$	EULER angles vector of the body $\mathcal{B}$ computed at the point $P$ with respect to the inertial frame, expressed in rad and using the 'ZYX' sequence of rotations.
$\mathbf{F}_{\text{ext}/\mathcal{B},G}$	External forces vector applied to the body $\mathcal{B}$ at the point $G$ , expressed in N.
$\mathbf{T}_{\text{ext}/\mathcal{B},G}$	External torques vector applied to the body $\mathcal{B}$ at the point $G$ , expressed in N m.
$\mathbf{F}_{\mathcal{B}/\mathcal{A},G}$	Forces vector applied by the body $\mathcal{B}$ to the body $\mathcal{A}$ at the point $G$ , expressed in N.
$\mathbf{T}_{\mathcal{B}/\mathcal{A},G}$	Torques vector applied by the body $\mathcal{B}$ to the body $\mathcal{A}$ at the point $G$ , expressed in N m.
$\mathbf{W}_{\mathcal{B}/\mathcal{A},G}$	Wrench vector applied by the body $\mathcal{B}$ to the body $\mathcal{A}$ at the point $G$ : $\mathbf{W}_{\mathcal{B}/\mathcal{A},G} = \left[ \begin{array}{cc} \mathbf{F}_{\mathcal{B}/\mathcal{A},G}^T & \mathbf{T}_{\mathcal{B}/\mathcal{A},G}^T \end{array} \right]^T$ , expressed in [N N m].
$[\mathbf{X}]_{\mathcal{R}_\bullet}$	$\mathbf{X}$ (model, vector or tensor) expressed in the frame $\mathcal{R}_\bullet$ .
$\mathbf{X}$	$\mathbf{X}$ (model, vector or tensor) expressed in the body frame, unless stated otherwise.
$\mathbf{m}_P^{\mathcal{B}}$	Motion vector of the body $\mathcal{B}$ at the point $P$ : $\mathbf{m}_P^{\mathcal{B}} = \left[ \begin{array}{cccccc} \dot{\mathbf{v}}_P^{\mathcal{B}T} & \dot{\boldsymbol{\omega}}_P^{\mathcal{B}T} & \mathbf{v}_P^{\mathcal{B}T} & \boldsymbol{\omega}_P^{\mathcal{B}T} & \mathbf{x}_P^T & \boldsymbol{\Theta}_P^{\mathcal{B}T} \end{array} \right]^T$ .
$\mathbf{P}_{\mathcal{R}_a/\mathcal{R}_b}$	DCM from the frame $\mathcal{R}_a$ to the frame $\mathcal{R}_b$ ( $[\mathbf{v}]_{\mathcal{R}_b} = \mathbf{P}_{\mathcal{R}_a/\mathcal{R}_b} [\mathbf{v}]_{\mathcal{R}_a}$ for any vector $\mathbf{v}$ ).
$\mathbf{P}_{\mathcal{R}_b/\mathcal{R}_i} = \text{DCM}(\boldsymbol{\Theta}^{\mathcal{B}})$	Function that computes the DCM from the EULER angles vector of a rigid body $\mathcal{B}$ .
$\mathbf{I}_n$	Identity matrix $n \times n$ .
$\mathbf{0}_{n \times m}$	Zero matrix $n \times m$ .
$\mathbf{v}\{i\}$	Component $i$ of vector $\mathbf{v}$ .
$(*\mathbf{v})$	Skew symmetric matrix associated with vector $\mathbf{v}$ : $[(*\mathbf{v})]_{\mathcal{R}_\bullet} = \left[ \begin{array}{ccc} 0 & -\mathbf{v}\{3\} & \mathbf{v}\{2\} \\ \mathbf{v}\{3\} & 0 & -\mathbf{v}\{1\} \\ -\mathbf{v}\{2\} & \mathbf{v}\{1\} & 0 \end{array} \right]_{\mathcal{R}_\bullet}$ .
$\boldsymbol{\tau}_{PB}$	Kinematic model between the points $P$ and $B$ : $[\boldsymbol{\tau}_{PB}]_{\mathcal{R}_\bullet} = \left[ \begin{array}{cc} \mathbf{I}_3 & (*\mathbf{PB}) \\ \mathbf{0}_{3 \times 3} & \mathbf{I}_3 \end{array} \right]_{\mathcal{R}_\bullet}$ .
$\mathbf{u} \wedge \mathbf{v}$	Cross product of vectors $\mathbf{u}$ and $\mathbf{v}$ ( $\mathbf{u} \wedge \mathbf{v} = (*\mathbf{u}) \mathbf{v}$ ).
$\ \mathbf{v}\ _2$	Euclidean norm of the vector $\mathbf{v}$ .
$\hat{\mathbf{v}} = \frac{\mathbf{v}}{\ \mathbf{v}\ _2}$	Normalized vector $\hat{\mathbf{v}}$ of a non-zero vector $\mathbf{v}$ (or unit vector in the direction of $\mathbf{v}$ ).
$\Phi'(x)$	Derivative of $\Phi(x)$ with respect to the spatial derivative $x$ .
$\dot{\mathbf{x}}(t)$	First time derivative of $\mathbf{x}$ with respect to the body frame.
$\mathbf{X}_{(\mathbf{I},\mathbf{J})}$	Subsystem of $\mathbf{X}$ from the inputs indexed in the vector $\mathbf{J}$ to the outputs indexed in the vector $\mathbf{I}$ (if $(\mathbf{I}, \mathbf{J}) = (:, 7 : 10)$ , it means that one is considering the subsystem between the inputs from 7 until 10 to all the outputs).

$\text{diag}(\mathbf{A}, \mathbf{B}, \dots)$	Block-diagonal augmented matrix.
$\bar{\mathbf{x}}$	Equilibrium value of $\mathbf{x}$ .
$\delta\mathbf{x}$	Small variation of $\mathbf{x}$ around a defined equilibrium.
$\mathbf{J}_G^{\mathcal{B}}$	Inertia tensor of $\mathcal{B}$ , computed at the point $G$ , written in $\mathcal{R}_b$ and expressed in $\text{kg m}^2$ .
$m^{\mathcal{B}}$	Mass of $\mathcal{B}$ expressed in kg.
$s$	LAPLACE'S variable.

## 1. Introduction

### 1.1. Background and motivation

The design of helicopter rotor systems, wind turbines and various other devices has motivated numerous studies into the flexural vibration modes of rotating beams [1]. The use of structures that can be modeled as a rotating beam is also very common in spacecraft applications, which usually employ long, flexible and rotating space booms [2] or high gain antennas. Some examples are the Cluster mission [3] and the Turbulence Heating Observer (THOR) satellite mission proposal [4]. On this basis, it is not surprising that there is extensive literature concerning the dynamics and vibrations of such structures [5]. Traditionally, these components were designed using rigid materials. However, the current trend is to employ more flexible and lightweight structures. This trend is particularly significant in space missions.

Numerous previous studies have focused on the analysis of non-rotating non-uniform blades [6, 7, 8, 9]. In particular, Auciello *et al.* [6] and Zhou *et al.* [7] employed the Rayleigh-Ritz method to investigate the vibration behavior of non-uniform Euler-Bernoulli beams with polynomial cross-sections, incorporating discrete elements to account for moment of inertia variations and different boundary conditions. Recent studies have also utilized the homotopy perturbation transform method [9, 10, 11, 12, 13] to address the same problem.

Moreover, several research groups have conducted studies using the Adomian decomposition method and the Adomian Modified Decomposition Method (AMDM) for uniform beams, according to either the Euler-Bernoulli or the Timoshenko formulations [14, 15, 16, 17]. Mao [14] utilized the AMDM for rotating uniform beams, incorporating a centrifugal stiffening term, while Hsu *et al.* [15] applied the AMDM to Timoshenko beams. Khan *et al.* [18] demonstrated the potential for enhanced accuracy in AMDM solutions by incorporating Green functions. Recent studies have also explored the analysis of rotating cantilever beams and related nonlinear oscillations in structural engineering [19, 20, 21]. Additionally, Adair *et al.* [22] employed the AMDM to analyze the free transverse vibration of rotating non-uniform Euler-Bernoulli beams, considering various boundary conditions, rotation speeds and beam lengths. Previous studies [23, 1, 24] have generally utilized the Euler-Bernoulli beam theory and employed various approximate solution techniques to determine the dynamic characteristics of such rotating beams. Yoo *et al.* [25] specifically investigated the influence of the centrifugal force and utilized a modal formulation to determine the natural frequencies. Furthermore, other methods have also been used to compute the natural frequencies of rotating beams in [26, 27, 28, 29, 30].

From the perspective of the Attitude and Orbit Control System (AOCS) and Guidance, Navigation, and Control (GNC), the challenges associated with spinning spacecraft missions arise primarily due to the impact of centrifugal stiffening on the dynamics of the satellite's flexible rotating booms. Therefore, the success of such missions relies heavily on the ability to develop an accurate system model. In this context, the comprehensive modeling of complex multibody structures becomes crucial as it enables the prediction of worst-case scenarios early on and offers the capacity to push the control system to its performance limits. Furthermore, having a model that is valid for any possible configuration simplifies the synthesis of the controller, eliminating the need for frequent switching between control modes. The transition between different control phases poses a critical aspect in control design, often involving intermediate tranquilization time windows. Consequently, the objective of this paper is not only to achieve an accurate model that characterizes the flexible modes of a rotating beam but also to construct a model which can be integrated in a multibody flexible system that facilitates robust control design and analysis.

In multibody dynamics, link flexibility is usually approximated using finite element methods (FEM) or assumed mode methods (AMM) [31] and the complete system model is derived using the Euler-Lagrange formalism. For space applications with a flexible robotic arm on a chaser spacecraft, the AMM approach is commonly used [31, 32], considering the first clamped-mass eigenfunctions. However, when dealing with scenarios like capturing massive

space debris, the boundary conditions at the flexible link tips may resemble clamped-clamped rather than clamped-mass conditions. Therefore, it is very important to have valid models for each link or substructure under arbitrary boundary conditions prior to assembling the entire structure. The transfer matrix method (TMM) has been extensively researched in substructuring approaches, establishing a relationship between state vectors at different points of a flexible body [33]. It has proven effective for modeling structures with serially connected bodies or open-chain-like structures. The TMM has been combined with the finite element (FE) method, leading to the FE-TM method [34], enabling reduced models, handling complex-shaped bodies and reducing computational efforts [35, 36]. Extensions have been developed for control design, including non-collocated feedback [37, 38], and for hybrid multibody systems with both rigid and flexible components [39]. However, the TMM has limitations. Inverting submatrices can be challenging when dealing with non-square or non-invertible matrices, depending on the boundary conditions [37]. Moreover, the TMM cannot be directly applied to tree-like structures, such as a spacecraft with a main rigid body and multiple flexible appendages. In these cases, establishing a relationship between generalized forces and displacements at the root of the structure is crucial for designing the AOCs. Efficient approaches have been developed to address this scenario, such as the effective mass/inertia model for each appendage or the utilization of the impedance matrix [40]. These methods, commonly employed in space engineering, analyze dynamic coupling between substructures using component mode synthesis (CMS) [41]. However, the effective mass/inertia approach has limitations as it loses information about the appendage beyond the attachment point, such as the deflection at the free tip. Therefore, it cannot accurately model arbitrary chain-like structures with flexible bodies.

The main contribution of this paper is to propose a methodology for modeling the six degrees of freedom (DOF) linear dynamic behavior of a flexible rotating Euler-Bernoulli beam within a multibody system, which includes the analysis of vibration in rotating uniform cantilever beams with a central hub and tip mass. The proposed model is built using the Two-Input-Two-Output Port (TITOP) approach [42], which considers forces and accelerations at the connection points as inputs and outputs. Unlike traditional methods, this approach is not reliant on specific boundary conditions at the connection points of the link. By integrating direct and inverse dynamic models in a concise state-space representation, the TITOP model ensures invertible input-output channels. This allows for seamless integration into the overall multibody system model, treating it as a block-diagram model. The boundary conditions at the connection points are treated as external feedback loops between forces and accelerations. This approach also offers the possibility to model complex multibody mechanical systems, while keeping the uncertain nature of the plant and condensing all the possible mechanical configurations in a single Linear Fractional Representation (LFR). The TITOP model effectively bridges the gap between the transfer matrix method and the effective mass-inertia method. This approach has been previously introduced in [42] and has found practical applications in space engineering, as demonstrated in [43, 44, 45, 46, 47, 48]. The beam model is derived using the Lagrange technique combined with a finite element model which considers fifth-order polynomial shape functions [49]. The obtained LFR model is characterized by its parameterization with respect to the angular velocity, resulting in a Linear Parameter-Varying (LPV) system that accommodates the centrifugal stiffening effect.

The models constructed using the TITOP approach are well-suited for robust control synthesis, as well as robust performance assessment. Additionally, all the models developed with the TITOP approach have been integrated into the most recent release of the Satellite Dynamics Toolbox library (SDTlib) [50].

The paper also includes a case study involving a spinning spacecraft, where the spacecraft's design is inspired by the THOR and Cluster missions. The main equipment platform is located around a central rigid body. Two flexible booms, resembling long rods, are connected to the rigid hub of the spacecraft. These booms become active when the spacecraft starts spinning. Their purpose can be to measure the varying electrical and magnetic fields surrounding the spacecraft (Cluster mission) or to carry plasma measurement instruments at their tips (THOR project). In this paper, these measurement instruments will be treated as tip masses.

## 1.2. Contributions and paper organization

The paper introduces the following key contributions:

- the development of a six DOF analytical two-port model of a spinning, flexible and uniform Euler-Bernoulli beam, fully capturing the bending, traction and torsion dynamics in a single LFR. Furthermore, this LPV model is parameterized according to the angular velocity of the beam, which facilitates robust control design.

- the validation of the TITOP six DOF beam model, by comparing the natural frequencies with a commercial finite element software. This analysis pretends to fill a gap in the literature since the authors did not find any results regarding the natural frequencies of a flexible, spinning, cantilever and uniform six DOF beam for the different conditions presented in this paper.
- the illustration in tables of the frequency ratios associated with the beam's different dynamics.
- the multibody modeling and analysis of a spinning satellite mission scenario composed of one main central body, two flexible booms and two tip masses.

This paper is organized into five parts. In the first part (section 2), an introduction to the TITOP approach is provided and the scope of the proposed model is discussed, together with some generalities. In the second part (section 3), the spinning rigid body dynamics are derived. In the third part of the paper (section 4), the analytical two-port model of a spinning, flexible and uniform beam taking into account a hub radius and a tip mass is computed. Finally, the fourth part (section 5) showcases a model validation and thorough analysis of all the obtained results, while the fifth part (section 6) details the rigorous modeling procedure of a spinning spacecraft mission scenario.

## 2. Scope of the proposed model and generalities

One of the objectives of this paper is to develop a generic multibody system modeling tool dedicated to the dynamics of spinning spacecraft composed of several rigid and flexible appendages. A general sketch of such a satellite, inspired by previous space missions like Cluster and THOR, is depicted in Fig. 1. This spacecraft comprises the main body  $\mathcal{B}$  and various links  $\mathcal{A}_i$ . Each body  $\mathcal{A}_i$  is connected to a parent substructure  $\mathcal{A}_{i-1}$  at the point  $P_i$  and to a child substructure  $\mathcal{A}_{i+1}$  at the point  $C_i$ . Without loss of generality, it is assumed that the spin axis of the main body  $\mathcal{B}$  is along the  $\mathbf{z}_b$ -axis of its body frame  $\mathcal{R}_b$ .

### 2.1. Assumptions

The following assumptions are taken into account throughout this work:

- the proposed model considers any rigid appendages or substructures but flexible appendages or substructures are restricted to Euler-Bernoulli beams.
- only the linear behavior of the spacecraft is addressed; i.e., only small motions and deformations around an equilibrium are considered.
- the considered equilibrium is stable. This implies that the spacecraft is symmetric around its spin axis  $\mathbf{z}_b$  and that this axis does not correspond to the intermediate principal moment of inertia of the satellite, in order to avoid the DZHANIBEKOV effect [51].
- the static deformations of flexible beams due to centrifugal loads are small and neglected in the computation of the equilibrium conditions. Note that these static deformations can be evaluated to verify this assumption, as proposed in section 4.
- zero-gravity environment.

Under these assumptions, it is possible to compute for each body  $\mathcal{A}_i$  the equilibrium conditions which are characterized by:

- $\bar{\mathbf{v}}_{P_i}^{\mathcal{A}_i}$  and  $\bar{\boldsymbol{\omega}}_{P_i}^{\mathcal{A}_i}$ : the linear and angular velocity vectors of the body  $\mathcal{A}_i$  at the point  $P_i$ .
- $\bar{\mathbf{W}}_{\mathcal{A}_{i+1}/\mathcal{A}_i, C_i} = \left[ \bar{\mathbf{F}}_{\mathcal{A}_{i+1}/\mathcal{A}_i, C_i}^T, \bar{\mathbf{T}}_{\mathcal{A}_{i+1}/\mathcal{A}_i, C_i}^T \right]^T$ : the wrench applied by the child substructure  $\mathcal{A}_{i+1}$  to the current body  $\mathcal{A}_i$  at the connection point  $C_i$  due to centrifugal loads.

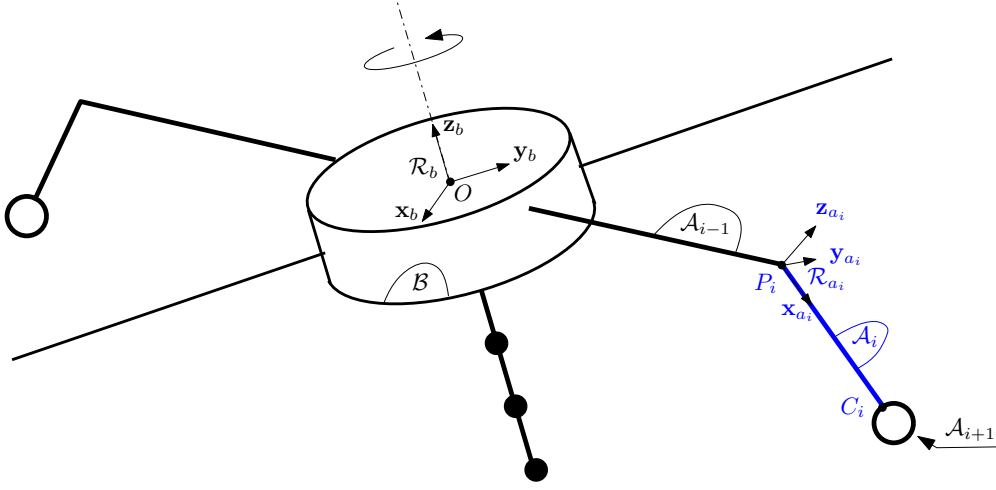


Figure 1: A spinning satellite with various rigid and/or flexible appendages.

## 2.2. TITOP approach with motion vectors

The TITOP approach that has been previously presented in [42, 43, 44, 45, 46, 47, 48] links the 6 components of the interaction wrenches to the 6 components of the inertial acceleration dual vectors at the points  $P_i$  and  $C_i$ , assuming small motions around null equilibrium conditions. To linearize the model of a spinning satellite around non-null kinematic equilibrium conditions ( $\overline{\mathbf{v}}_{P_i}^{\mathcal{A}_i}$  and  $\overline{\boldsymbol{\omega}}_{P_i}^{\mathcal{A}_i}$ ), the TITOP model developed hereafter considers the 18-components motion vectors  $\mathbf{m}_{P_i}^{\mathcal{A}_i}$  and  $\mathbf{m}_{C_i}^{\mathcal{A}_i}$ , as defined in the nomenclature, as well as their corresponding equilibrium values and variations. For example, it follows that:

$$\mathbf{m}_{P_i}^{\mathcal{A}_i} = \underbrace{\begin{bmatrix} \mathbf{0}_{1 \times 6}, \mathbf{0}_{1 \times 6}, \overline{\mathbf{v}}_{P_i}^{\mathcal{A}_i}, \overline{\boldsymbol{\omega}}_{P_i}^{\mathcal{A}_i}, \overline{\mathbf{x}}_{P_i}^{\mathcal{A}_i}, \overline{\boldsymbol{\Theta}}_{P_i}^{\mathcal{A}_i} \end{bmatrix}^T}_{\overline{\mathbf{m}}_{P_i}^{\mathcal{A}_i}} + \underbrace{\begin{bmatrix} \delta \overline{\mathbf{v}}_{P_i}^{\mathcal{A}_i}, \delta \overline{\boldsymbol{\omega}}_{P_i}^{\mathcal{A}_i}, \delta \overline{\mathbf{x}}_{P_i}^{\mathcal{A}_i}, \delta \overline{\boldsymbol{\Theta}}_{P_i}^{\mathcal{A}_i} \end{bmatrix}^T}_{\delta \mathbf{m}_{P_i}^{\mathcal{A}_i}} \quad (1)$$

Similarly, since the wrench  $\overline{\mathbf{W}}_{\mathcal{A}_{i+1}/\mathcal{A}_i, C_i}$  applied at the point  $C_i$  at the equilibrium is no longer null, the linear TITOP model must now consider the deformed body frame  $\mathcal{R}_{a_i(C_i)}$  attached to the body  $\mathcal{A}_i$  at the point  $C_i$ , in addition to the "rigid" body frame  $\mathcal{R}_{a_i}$  attached to the body  $\mathcal{A}_i$  at the point  $P_i$ , as depicted in Fig. 2a.

Therefore, the double-port or TITOP model  $\left[ \mathfrak{T}_{P_i, C_i}^{\mathcal{A}_i}(s) \right]_{\mathcal{R}_{a_i}}$  of the body  $\mathcal{A}_i$  is a linear dynamic model between 24 inputs:

- the six components of the wrench variation  $[\delta \mathbf{W}_{\mathcal{A}_{i+1}/\mathcal{A}_i, C_i}]_{\mathcal{R}_{a_i(C_i)}}$  applied by the child substructure  $\mathcal{A}_{i+1}$  to the body  $\mathcal{A}_i$  at the point  $C_i$ , expressed in the deformed body frame  $\mathcal{R}_{a_i(C_i)}$ .
- the eighteen components of the motion vector variation  $[\delta \mathbf{m}_{P_i}^{\mathcal{A}_i}]_{\mathcal{R}_{a_i}}$  defined at the point  $P_i$  and expressed in the rigid body frame  $\mathcal{R}_{a_i}$ .

and 24 outputs:

- the eighteen components of the motion vector variation  $[\delta \mathbf{m}_{C_i}^{\mathcal{A}_i}]_{\mathcal{R}_{a_i(C_i)}}$  defined at the point  $C_i$  and expressed in the deformed body frame  $\mathcal{R}_{a_i(C_i)}$ .
- the six components of the wrench variation  $[\delta \mathbf{W}_{\mathcal{A}_i/\mathcal{A}_{i-1}, P_i}]_{\mathcal{R}_{a_i}}$  that is applied by the body  $\mathcal{A}_i$  to the parent substructure  $\mathcal{A}_{i-1}$  at the point  $P_i$ , expressed in the rigid body frame  $\mathcal{R}_{a_i}$ .

and can be represented by the block-diagram depicted in Fig. 2b. The TITOP model is composed of the direct dynamic model (transfer from motion vector variation to wrench variation) at the point  $P_i$  and the inverse dynamic model (transfer from wrench variation to motion vector variation) at the point  $C_i$ . This model depends on the kinematic equilibrium conditions  $\left[ \bar{\mathbf{v}}_{P_i}^{\mathcal{A}_i}, \bar{\boldsymbol{\omega}}_{P_i}^{\mathcal{A}_i} \right]^T$  at the point  $P_i$  and the equilibrium wrench at the point  $C_i$   $\left[ \bar{\mathbf{W}}_{\mathcal{A}_{i+1}/\mathcal{A}_i, C_i} \right]_{\mathcal{R}_{a_i(C_i)}} = \left[ \bar{\mathbf{W}}_{\mathcal{A}_{i+1}/\mathcal{A}_i, C_i} \right]_{\mathcal{R}_{a_i}}$ . Indeed, at the equilibrium and under the adopted assumptions, the frames  $\mathcal{R}_{a_i}$  and  $\mathcal{R}_{a_i(C_i)}$  are aligned. It should also be noted that the equilibrium conditions can be propagated forward (from parent to child) to provide  $\left[ \bar{\mathbf{v}}_{C_i}^{\mathcal{A}_i}, \bar{\boldsymbol{\omega}}_{C_i}^{\mathcal{A}_i} \right]^T$  and backwards (from child to parent) to provide  $\left[ \bar{\mathbf{W}}_{\mathcal{A}_i/\mathcal{A}_{i-1}, P_i} \right]_{\mathcal{R}_{a_i}}$ .

Moreover, Eq. (1) also introduced the geometric equilibrium conditions  $\left[ \bar{\mathbf{x}}_{P_i}^{\mathcal{A}_i}, \bar{\boldsymbol{\Theta}}_{P_i}^{\mathcal{A}_i} \right]^T$ . However, the dynamics of the various TITOP models developed hereafter do not depend on these geometric conditions. For this reason, they do not appear on the block-diagram depicted in Fig. 2b.

Ultimately, the subscript  $i$  will be omitted hereafter and the substructures (parent or child) connected to the body in question will be denoted as  $\bullet$  for brevity. Similarly, the equilibrium signals (represented in green in Fig. 2b) will not be displayed in the block-diagrams presented henceforth.

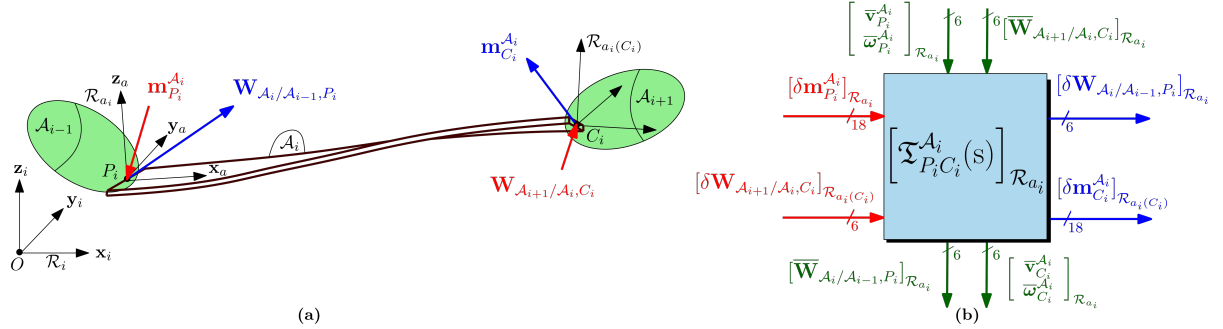


Figure 2: (a) Three-Dimensional (3D) representation of a flexible spinning beam  $\mathcal{A}_i$ . (b) TITOP model  $\left[ \mathfrak{T}_{P_i, C_i}^{\mathcal{A}_i}(s) \right]_{\mathcal{R}_{a_i}}$  block-diagram.

### 2.3. LAGRANGE equations in terms of quasi-coordinates

The TITOP models derived in the following sections are based on the LAGRANGE equations in terms of quasi-coordinates [52], which are rewritten here in the non-dissipative case:

$$\frac{d}{dt} \frac{\partial \mathcal{L}}{\partial \begin{bmatrix} \delta \mathbf{v}_P^{\mathcal{A}} \\ \delta \boldsymbol{\omega}_P^{\mathcal{A}} \end{bmatrix}_{\mathcal{R}_a}} + \begin{bmatrix} (*\boldsymbol{\omega}_P^{\mathcal{A}}) & \mathbf{0}_{3 \times 3} \\ (*\mathbf{v}_P^{\mathcal{A}}) & (*\boldsymbol{\omega}_P^{\mathcal{A}}) \end{bmatrix}_{\mathcal{R}_a} \frac{\partial \mathcal{L}}{\partial \begin{bmatrix} \delta \mathbf{v}_P^{\mathcal{A}} \\ \delta \boldsymbol{\omega}_P^{\mathcal{A}} \end{bmatrix}_{\mathcal{R}_a}} - \begin{bmatrix} \mathbf{0}_{3 \times 3} & \mathbf{0}_{3 \times 3} \\ \mathbf{0}_{3 \times 3} & \boldsymbol{\Gamma}^{-T}(\boldsymbol{\Theta}_P^{\mathcal{A}}) \end{bmatrix} \frac{\partial \mathcal{L}}{\partial \begin{bmatrix} \delta \mathbf{x}_P^{\mathcal{A}} \\ \delta \boldsymbol{\Theta}_P^{\mathcal{A}} \end{bmatrix}_{\mathcal{R}_a}} = \begin{bmatrix} \mathbf{F}_{\text{ext}/\mathcal{A}, P} \\ \mathbf{T}_{\text{ext}/\mathcal{A}, P} \end{bmatrix}_{\mathcal{R}_a} \quad (2)$$

$$\frac{d}{dt} \frac{\partial \mathcal{L}}{\partial \delta \mathbf{q}_f} - \frac{\partial \mathcal{L}}{\partial \delta \mathbf{q}_f} = \widehat{\mathbf{U}} \quad (3)$$

In Eq. (2),  $\mathcal{L} = \mathcal{T} - \mathcal{V}$  is the Lagrangian, where  $\mathcal{T}$  and  $\mathcal{V}$  are the kinetic and potential energies, respectively. Furthermore,  $\boldsymbol{\Gamma}(\boldsymbol{\Theta}_P^{\mathcal{A}})$  represents the mapping between the angular velocity vector and the time derivative of the EULER angles vector [53], with  $[\boldsymbol{\omega}_P^{\mathcal{A}}]_{\mathcal{R}_a} = \boldsymbol{\Gamma}(\boldsymbol{\Theta}_P^{\mathcal{A}}) \dot{\boldsymbol{\Theta}}_P^{\mathcal{A}}$ . Eq. (2) is related to the 6 rigid DOF (3 translations and 3 rotations) of the body, while Eq. (3) is related to the internal elastic deformations. The right-hand sides of Eqs. (2) and (3) are composed of the resultant wrench  $[\mathbf{W}_{\text{ext}/\mathcal{A}, P}]_{\mathcal{R}_a} = [\mathbf{F}_{\text{ext}/\mathcal{A}, P}^T, \mathbf{T}_{\text{ext}/\mathcal{A}, P}^T]_{\mathcal{R}_a}^T$  applied to the body  $\mathcal{A}$  at the point  $P$  and the nonconservative generalized forces  $\widehat{\mathbf{U}}$  associated with the elastic motions. Finally,  $\mathbf{q}_f$  are distributed coordinates describing elastic motions relative to the rigid body motions.

### 3. Analytical two-port model of a spinning rigid body

#### 3.1. Case of a rigid appendage

For a rigid body  $\mathcal{A}$  that is free to move in space, the frames  $\mathcal{R}_a$  and  $\mathcal{R}_{a(C)}$  are always aligned. Besides that, gravity is not taken into account, meaning that:

$$\mathcal{L} = \mathcal{T} = \frac{1}{2} \begin{bmatrix} \mathbf{v}_P^{\mathcal{A}} \\ \boldsymbol{\omega}_P^{\mathcal{A}} \end{bmatrix}^T \mathbf{D}_P^{\mathcal{A}} \begin{bmatrix} \mathbf{v}_P^{\mathcal{A}} \\ \boldsymbol{\omega}_P^{\mathcal{A}} \end{bmatrix} \quad (4)$$

It should be noted that all the quantities in Eq. (4) are projected in the body frame  $\mathcal{R}_a$  (omitted for brevity).  $\mathbf{D}_P^{\mathcal{A}}$  is the  $6 \times 6$  direct rigid dynamic model of the body  $\mathcal{A}$  at the point  $P$ , which can be computed from the dynamic model  $\mathbf{D}_A^{\mathcal{A}}$  written at the body's center of mass  $A$  and the kinematic model  $\boldsymbol{\tau}_{AP}$  (see nomenclature):

$$\mathbf{D}_P^{\mathcal{A}} = \boldsymbol{\tau}_{AP}^T \underbrace{\begin{bmatrix} m^{\mathcal{A}} \mathbf{I}_3 & \mathbf{0}_{3 \times 3} \\ \mathbf{0}_{3 \times 3} & \mathbf{J}_A^{\mathcal{A}} \end{bmatrix}}_{\mathbf{D}_A^{\mathcal{A}}} \boldsymbol{\tau}_{AP} = \begin{bmatrix} m^{\mathcal{A}} \mathbf{I}_3 & m^{\mathcal{A}} (*\mathbf{AP}) \\ -m^{\mathcal{A}} (*\mathbf{AP}) & \underbrace{\mathbf{J}_A^{\mathcal{A}} - m^{\mathcal{A}} (*\mathbf{AP})^2}_{\mathbf{J}_P^{\mathcal{A}}} \end{bmatrix} \quad (5)$$

Considering that the body  $\mathcal{A}$  is only subjected to the interaction wrenches at the points  $P$  and  $C$ , the direct application of Eq. (2) leads to the following non-linear model:

$$\mathbf{D}_P^{\mathcal{A}} \begin{bmatrix} \dot{\mathbf{v}}_P^{\mathcal{A}} \\ \dot{\boldsymbol{\omega}}_P^{\mathcal{A}} \end{bmatrix} + \begin{bmatrix} (*\boldsymbol{\omega}_P^{\mathcal{A}}) & \mathbf{0}_{3 \times 3} \\ (*\mathbf{v}_P^{\mathcal{A}}) & (*\boldsymbol{\omega}_P^{\mathcal{A}}) \end{bmatrix} \mathbf{D}_P^{\mathcal{A}} \begin{bmatrix} \mathbf{v}_P^{\mathcal{A}} \\ \boldsymbol{\omega}_P^{\mathcal{A}} \end{bmatrix} = -\mathbf{W}_{\mathcal{A}/\bullet,P} + \boldsymbol{\tau}_{CP}^T \mathbf{W}_{\bullet/\mathcal{A},C} \quad (6)$$

Given the equilibrium conditions  $\bar{\mathbf{v}}_P^{\mathcal{A}}$ ,  $\bar{\boldsymbol{\omega}}_P^{\mathcal{A}}$  and  $\bar{\mathbf{W}}_{\bullet/\mathcal{A},C}$ , one can compute the equilibrium wrench at the point  $P$ :

$$\bar{\mathbf{W}}_{\mathcal{A}/\bullet,P} = \boldsymbol{\tau}_{CP}^T \bar{\mathbf{W}}_{\bullet/\mathcal{A},C} - \begin{bmatrix} (*\bar{\boldsymbol{\omega}}_P^{\mathcal{A}}) & \mathbf{0}_{3 \times 3} \\ (*\bar{\mathbf{v}}_P^{\mathcal{A}}) & (*\bar{\boldsymbol{\omega}}_P^{\mathcal{A}}) \end{bmatrix} \mathbf{D}_P^{\mathcal{A}} \begin{bmatrix} \bar{\mathbf{v}}_P^{\mathcal{A}} \\ \bar{\boldsymbol{\omega}}_P^{\mathcal{A}} \end{bmatrix} \quad (7)$$

After performing some algebraic operations based on the properties of the skew symmetric matrix, the first-order linearized model becomes:

$$\mathbf{D}_P^{\mathcal{A}} \begin{bmatrix} \delta \dot{\mathbf{v}}_P^{\mathcal{A}} \\ \delta \dot{\boldsymbol{\omega}}_P^{\mathcal{A}} \end{bmatrix} + \underbrace{\begin{bmatrix} m^{\mathcal{A}} (*\bar{\boldsymbol{\omega}}_P^{\mathcal{A}}) & m^{\mathcal{A}} (2(*\bar{\boldsymbol{\omega}}_P^{\mathcal{A}})(*\mathbf{AP}) - (*\mathbf{AP})(*\bar{\boldsymbol{\omega}}_P^{\mathcal{A}}) - (*\bar{\mathbf{v}}_P^{\mathcal{A}})) \\ -m^{\mathcal{A}} (*\mathbf{AP})(*\bar{\boldsymbol{\omega}}_P^{\mathcal{A}}) & m^{\mathcal{A}} (*\mathbf{AP})(*\bar{\mathbf{v}}_P^{\mathcal{A}}) + (*\bar{\boldsymbol{\omega}}_P^{\mathcal{A}}) \mathbf{J}_P^{\mathcal{A}} - (*\mathbf{J}_P^{\mathcal{A}} \bar{\boldsymbol{\omega}}_P^{\mathcal{A}}) \end{bmatrix}}_{\mathbf{X}_P^{\mathcal{A}}(\bar{\mathbf{v}}_P^{\mathcal{A}}, \bar{\boldsymbol{\omega}}_P^{\mathcal{A}})} \begin{bmatrix} \delta \mathbf{v}_P^{\mathcal{A}} \\ \delta \boldsymbol{\omega}_P^{\mathcal{A}} \end{bmatrix} = -\delta \mathbf{W}_{\mathcal{A}/\bullet,P} + \boldsymbol{\tau}_{CP}^T \delta \mathbf{W}_{\bullet/\mathcal{A},C} \quad (8)$$

In the context of a rigid body, the propagation of the variation of the motion vector from the point  $P$  to the point  $C$  simply reads:

$$\delta \mathbf{m}_C^{\mathcal{A}} = \underbrace{\text{diag}(\boldsymbol{\tau}_{CP}, \boldsymbol{\tau}_{CP}, \mathbf{I}_6)}_{\mathbf{v}_{CP}} \delta \mathbf{m}_P^{\mathcal{A}} \quad (9)$$

The block-diagram representation of the TITOP model  $\mathfrak{R}_{PC}^{\mathcal{A}}$  of the rigid body  $\mathcal{A}$  computed at the points  $P$  and  $C$  is summarized in Fig. 3. This linear model is static and does not depend on the equilibrium wrench  $\bar{\mathbf{W}}_{\bullet/\mathcal{A},C}$ , which will no longer be the case for the TITOP model of a spinning flexible beam, as the one presented in section 4. Furthermore, one can also define the one-port model of the rigid body  $\mathcal{A}$  at the point  $P$  in case there is no child substructure connected to it, with  $\mathfrak{R}_P^{\mathcal{A}} = \mathfrak{R}_{PC(19:24,7:24)}^{\mathcal{A}}$ .

### 3.2. Case of the rigid main body

For the particular case of the main body  $\mathcal{B}$  represented in Fig. 1, one has to consider the inverse dynamic model (transfer from wrench variation to the motion vector variation) written at the body's center of mass  $B$  and including the 6 rigid modes of the whole system. Thus, the model of the main body  $\mathcal{B}$  subjected to an external wrench and connected to several appendages  $\mathcal{A}_i$  at the points  $C_i$  reads:

$$\mathbf{D}_B^{\mathcal{B}} \begin{bmatrix} \delta \dot{\mathbf{v}}_B^{\mathcal{B}} \\ \delta \dot{\boldsymbol{\omega}}_B^{\mathcal{B}} \end{bmatrix} + \mathbf{X}_B^{\mathcal{B}}(\bar{\mathbf{v}}_B^{\mathcal{B}}, \bar{\boldsymbol{\omega}}_B^{\mathcal{B}}) \begin{bmatrix} \delta \mathbf{v}_B^{\mathcal{B}} \\ \delta \boldsymbol{\omega}_B^{\mathcal{B}} \end{bmatrix} = \delta \mathbf{W}_{\text{ext}/\mathcal{B},B} + \sum_i \boldsymbol{\tau}_{C_i B}^T \delta \mathbf{W}_{\mathcal{A}_i/\mathcal{B},C_i} \quad (10)$$

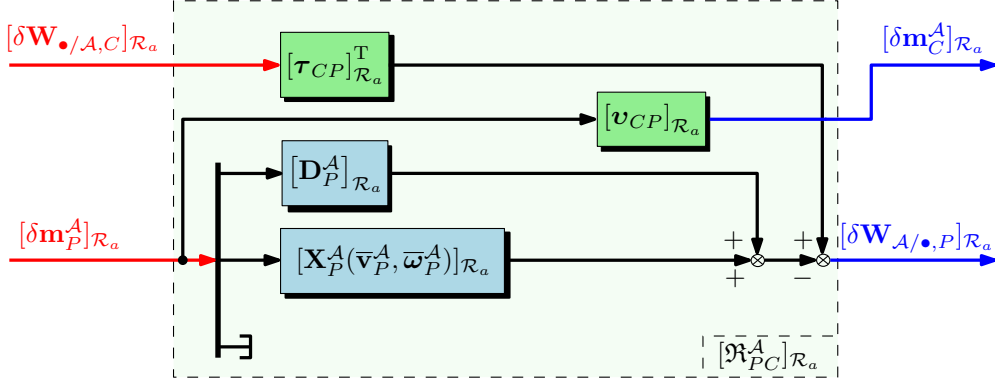


Figure 3: Block-diagram representation of  $[\mathfrak{R}_{PC}^{\mathcal{A}}]_{\mathcal{R}_a}$ : the linear  $24 \times 24$  model of a rigid body  $\mathcal{A}$  computed at the points  $P$  and  $C$ .

This model must then be completed with the following kinematic equation:

$$\begin{bmatrix} \dot{\mathbf{x}}_B^{\mathcal{B}} \\ \dot{\boldsymbol{\Theta}}_B^{\mathcal{B}} \end{bmatrix} = \begin{bmatrix} \frac{d\mathbf{x}_B^{\mathcal{B}}}{dt} \Big|_{\mathcal{R}_b} \\ \dot{\boldsymbol{\Theta}}_B^{\mathcal{B}} \end{bmatrix} = \begin{bmatrix} \mathbf{I}_3 & \begin{pmatrix} * \\ \mathbf{x}_B^{\mathcal{B}} \end{pmatrix} \\ \mathbf{0}_{3 \times 3} & \boldsymbol{\Gamma}^{-1}(\boldsymbol{\Theta}_B^{\mathcal{B}}) \end{bmatrix} \begin{bmatrix} \mathbf{v}_B^{\mathcal{B}} \\ \boldsymbol{\omega}_B^{\mathcal{B}} \end{bmatrix} \quad (11)$$

Without loss of generality, this equation is linearized around an equilibrium that is defined by:  $\bar{\mathbf{x}}_B^{\mathcal{B}} = \mathbf{0}_{3 \times 1}$ ,  $\bar{\boldsymbol{\omega}}_B^{\mathcal{B}} = [0, 0, \Omega]^T$  (the  $\mathbf{z}_b$ -axis is the spin axis) and  $\bar{\boldsymbol{\Theta}}_B^{\mathcal{B}} = [0, 0, \Omega t]^T$ , where the variable  $t$  represents the time. Then, considering the chosen 'ZYX' sequence of rotations for the EULER angles vector  $\boldsymbol{\Theta}_B^{\mathcal{B}} = [\delta\phi_B^{\mathcal{B}}, \delta\theta_B^{\mathcal{B}}, \psi_B^{\mathcal{B}}]^T$ , one can verify that  $\boldsymbol{\Gamma}(\boldsymbol{\Theta}_B^{\mathcal{B}})$  does not depend on  $\psi_B^{\mathcal{B}}$ , the spin angle, and write:

$$\boldsymbol{\Gamma}(\boldsymbol{\Theta}_B^{\mathcal{B}}) = \begin{bmatrix} 1 & 0 & -\sin \delta\theta_B^{\mathcal{B}} \\ 0 & \cos \delta\phi_B^{\mathcal{B}} & \sin \delta\phi_B^{\mathcal{B}} \cos \delta\theta_B^{\mathcal{B}} \\ 0 & -\sin \delta\phi_B^{\mathcal{B}} & \cos \delta\phi_B^{\mathcal{B}} \cos \delta\theta_B^{\mathcal{B}} \end{bmatrix} \approx \begin{bmatrix} 1 & 0 & -\delta\theta_B^{\mathcal{B}} \\ 0 & 1 & \delta\phi_B^{\mathcal{B}} \\ 0 & -\delta\phi_B^{\mathcal{B}} & 1 \end{bmatrix} \quad (12)$$

Consequently, the first-order linear kinematic model reads:

$$\begin{bmatrix} \delta \dot{\mathbf{x}}_B^{\mathcal{B}} \\ \delta \dot{\boldsymbol{\Theta}}_B^{\mathcal{B}} \end{bmatrix} = \begin{bmatrix} \delta \mathbf{v}_B^{\mathcal{B}} \\ \delta \boldsymbol{\omega}_B^{\mathcal{B}} \end{bmatrix} - \underbrace{\begin{bmatrix} (*\bar{\boldsymbol{\omega}}_B^{\mathcal{B}}) & \mathbf{0}_{3 \times 3} \\ \mathbf{0}_{3 \times 3} & (*\bar{\boldsymbol{\omega}}_B^{\mathcal{B}}) \end{bmatrix}}_{\mathbf{H}(\bar{\boldsymbol{\omega}}_B^{\mathcal{B}})} \begin{bmatrix} \delta \mathbf{x}_B^{\mathcal{B}} \\ \delta \boldsymbol{\Theta}_B^{\mathcal{B}} \end{bmatrix} \quad (13)$$

From Eqs. 10 and 13, the block-diagram representation of the twelfth-order model  $\mathfrak{X}_B^{\mathcal{B}}(s)$  of the main body  $\mathcal{B}$  written at its center of mass  $B$  can be obtained, as depicted in Fig. 4.

Finally, in order to assemble linear TITOP models between each other and/or to connect them to the main body, the DCM  $\mathbf{P}_{\mathcal{R}_a/\mathcal{R}_b}$  between the frame  $\mathcal{R}_a$  attached to the body  $\mathcal{A}$  and the frame  $\mathcal{R}_b$  attached to the body  $\mathcal{B}$  must be taken into account in the propagation of the wrench and motion vector variations. Let  $P$  be the point where  $\mathcal{A}$  is connected to  $\mathcal{B}$ . Then, it follows that:

$$[\delta \mathbf{W}_{\mathcal{A}/\mathcal{B},P}]_{\mathcal{R}_b} = \underbrace{\text{diag}(\mathbf{P}_{\mathcal{R}_a/\mathcal{R}_b}, \mathbf{P}_{\mathcal{R}_a/\mathcal{R}_b})}_{\mathbf{P}_{\mathcal{R}_a/\mathcal{R}_b}^{\times 2}} [\delta \mathbf{W}_{\mathcal{A}/\mathcal{B},P}]_{\mathcal{R}_a} \quad \text{and} \quad [\delta \mathbf{m}_P^{\mathcal{B}}]_{\mathcal{R}_b} = \underbrace{\text{diag}(\mathbf{P}_{\mathcal{R}_a/\mathcal{R}_b}^{\times 2}, \mathbf{P}_{\mathcal{R}_a/\mathcal{R}_b}^{\times 2}, \mathbf{P}_{\mathcal{R}_a/\mathcal{R}_b}^{\times 2})}_{\mathbf{P}_{\mathcal{R}_a/\mathcal{R}_b}^{\times 6}} [\delta \mathbf{m}_P^{\mathcal{A}}]_{\mathcal{R}_a} \quad (14)$$

Indeed, the DCM can also be applied to the variation of the EULER angles vector, since  $\text{DCM}(\delta \Theta) \approx \mathbf{I}_3 + (*\delta \Theta)$ . Then, the variation  $\delta \Theta_P^{\mathcal{B}}$  on the attitude of the body  $\mathcal{B}$  or the variation  $\delta \Theta_P^{\mathcal{A}}$  on the attitude of the body  $\mathcal{A}$  must have the same effect on the whole DCM between  $\mathcal{R}_a$  and  $\mathcal{R}_i$ :

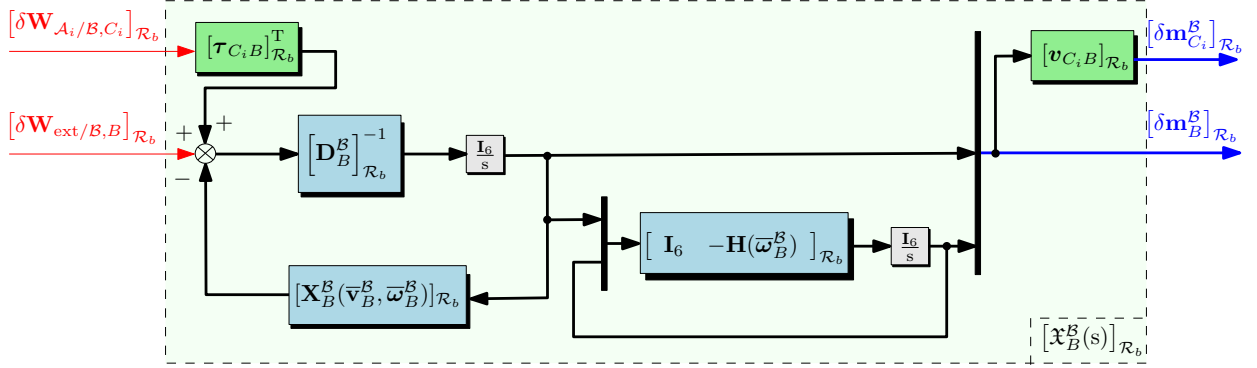


Figure 4: Detailed block-diagram representation of  $[\mathfrak{x}_B^{\mathcal{B}}(s)]_{\mathcal{R}_b}$ .

$$\begin{aligned} (\mathbf{I}_3 + (*\delta \Theta_P^{\mathcal{B}})) \mathbf{P}_{\mathcal{R}_a/\mathcal{R}_b} &= \mathbf{P}_{\mathcal{R}_a/\mathcal{R}_b} (\mathbf{I}_3 + (*\delta \Theta_P^{\mathcal{A}})) \Leftrightarrow (*\delta \Theta_P^{\mathcal{B}}) = \mathbf{P}_{\mathcal{R}_a/\mathcal{R}_b} (*\delta \Theta_P^{\mathcal{A}}) \mathbf{P}_{\mathcal{R}_a/\mathcal{R}_b}^T = (*(\mathbf{P}_{\mathcal{R}_a/\mathcal{R}_b} \delta \Theta_P^{\mathcal{A}})) \\ &\Leftrightarrow \delta \Theta_P^{\mathcal{B}} = \mathbf{P}_{\mathcal{R}_a/\mathcal{R}_b} \delta \Theta_P^{\mathcal{A}} \end{aligned} \quad (15)$$

All the elementary blocks and gains defined in this section ( $\mathfrak{x}_B^{\mathcal{B}}(s)$ ,  $\mathfrak{R}_P^{\mathcal{A}}$ ,  $\mathfrak{R}_{PC}^{\mathcal{A}}$ ,  $\mathbf{P}_{\mathcal{R}_a/\mathcal{R}_b}^{\times 6}$ ) can be used to build the model of the whole rigid system. Since all these blocks are analytically defined, it is possible to take into account uncertainties on the mechanical parameters of the system and also on the spin rate of the spacecraft by using the LFR formalism, as proposed in [44, 47, 48, 50]. In the following section, the TITOP modeling approach of spinning bodies is extended to flexible beams. Then, the way to use these elementary blocks is presented in section 6 (see Fig. 9 as an example).

#### 4. Analytical two-port model of a spinning, flexible and uniform Euler-Bernoulli beam

The objective of this section is to compute the TITOP model  $\mathfrak{Z}_{PC}^{\mathcal{A}}(s)$  of a spinning, flexible and uniform beam  $\mathcal{A}$ , as the one depicted in Fig. 2. This model will be first developed in the body frame  $\mathcal{R}_a$ . As a result, in this section, all the quantities are consistently projected in the frame  $\mathcal{R}_a$ , unless stated otherwise. For this reason, this frame is omitted in the notation for the sake of simplicity. Additionally, the deformed body frame  $\mathcal{R}_{a(C)}$  is introduced in section 4.4. This beam possesses various parameters, such as mass density  $\rho^{\mathcal{A}}$  ( $\text{kg m}^{-3}$ ), cross-sectional area  $S^{\mathcal{A}}$  ( $\text{m}^2$ ), length  $l^{\mathcal{A}}$  (m), Young's modulus  $E^{\mathcal{A}}$  ( $\text{N m}^{-2}$ ), Poisson's ratio  $\nu^{\mathcal{A}}$ , shear modulus  $G^{\mathcal{A}}$  ( $\text{N m}^{-2}$ ), with  $G^{\mathcal{A}} = \frac{E^{\mathcal{A}}}{2(1+\nu^{\mathcal{A}})}$ , second moment of area  $J_y^{\mathcal{A}}$  with respect to the  $\mathbf{y}_a$ -axis, second moment of area  $J_z^{\mathcal{A}}$  with respect to the  $\mathbf{z}_a$ -axis and second polar moment of area  $J_{px}^{\mathcal{A}}$  with respect to the  $\mathbf{x}_a$ -axis.

##### 4.1. Parametrization of the internal elastic deformations

The LAGRANGE technique combined with a finite element model which considers fifth-order polynomial shape functions [49] is used for obtaining the dynamic model of a flexible beam. In this approach, a moving body frame  $\mathcal{R}_a = (P; \mathbf{x}_a, \mathbf{y}_a, \mathbf{z}_a)$  is attached to the beam at the point  $P$ , as displayed in Fig. 2. Furthermore, Figs. 5a and 5b display the parameterization of the beam deflection at a given time  $t$  for two different cases: bending in the plane  $(P, \mathbf{x}_a, \mathbf{y}_a)$  and bending within the plane defined by  $(P, \mathbf{x}_a, \mathbf{z}_a)$ .

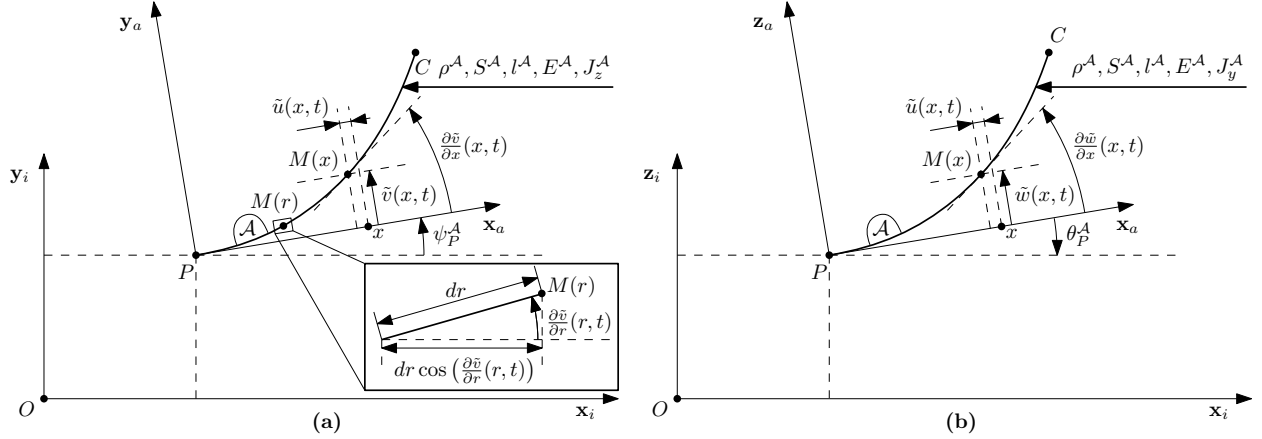


Figure 5: (a) Parameterization of the beam deflection at a given time  $t$  (Note: the displacement of a specific point  $M(x)$  on the deformed flexible beam  $u(x, t)$  along the  $\mathbf{x}_a$ -axis is displayed for both cases): (a) bending in the plane  $(P, \mathbf{x}_a, \mathbf{y}_a)$ . (b) bending in the plane  $(P, \mathbf{x}_a, \mathbf{z}_a)$ .

The deflections  $\tilde{v}(x, t)$  and  $\tilde{w}(x, t)$  in the moving frame  $\mathcal{R}_a$  are split up into  $N$  mode shapes  $\varphi_i^*(x)$  (for  $i = 1, \dots, N$ ), where  $\mathbf{\Phi}_*(x) = [\varphi_1^*(x), \dots, \varphi_N^*(x)]^T$  represents the mode shapes vectors. These vectors are linked with  $N$  time-varying variables  $q_i^*(t)$ , with  $\mathbf{q}_y(t) = [q_1^y(t), \dots, q_N^y(t)]^T$  and  $\mathbf{q}_z(t) = [q_1^z(t), \dots, q_N^z(t)]^T$ , as follows:

$$\tilde{v}(x, t) = \sum_{i=1}^N \varphi_i^y(x) q_i^y(t) = \mathbf{\Phi}_y^T(x) \mathbf{q}_y(t) \quad \text{and} \quad \tilde{w}(x, t) = \sum_{i=1}^N \varphi_i^z(x) q_i^z(t) = \mathbf{\Phi}_z^T(x) \mathbf{q}_z(t) \quad (16)$$

The mode shapes vectors which are used to model the beam dynamics in this paper are displayed in [Appendix A](#), where  $N = 4$ . Moreover, the inertial velocity  $\mathbf{v}_M^{\mathcal{A}}$  projected in the body frame and defined at a general point  $M(x)$  can be computed as follows:

$$\mathbf{v}_M^{\mathcal{A}} = \left. \frac{d\mathbf{OM}}{dt} \right|_{\mathcal{R}_i} = \left. \frac{d\mathbf{OP}}{dt} \right|_{\mathcal{R}_i} + \left. \frac{d\mathbf{PM}}{dt} \right|_{\mathcal{R}_a} + \omega_P^{\mathcal{A}} \wedge \mathbf{PM}, \quad \text{with} \quad \mathbf{OP} \equiv \mathbf{x}_P^{\mathcal{A}} \quad \text{and} \quad \mathbf{OM} \equiv \mathbf{x}_M^{\mathcal{A}} \quad (17)$$

Furthermore, the distance vector  $\mathbf{PM}$  displayed in Eq. (17) can be computed as:

$$\mathbf{PM}(x, t) = \begin{bmatrix} x + \tilde{u}(x, t) + \Delta u(x, t) \\ \tilde{v}(x, t) \\ \tilde{w}(x, t) \end{bmatrix} \quad (18)$$

In Eq. (18), the variable  $\tilde{u}(x, t)$  represents the displacement of a specific point  $M(x)$  on the deformed flexible beam along the  $\mathbf{x}_a$ -axis and  $\Delta u(x, t)$  denotes the deformation of the beam along the  $\mathbf{x}_a$ -axis due to traction-compression. Simply put,  $\tilde{u}(x, t)$  measures the deviation of the point  $M(x)$  from its position when the beam is in its undeformed state. From Figs. 5a and 5b, it can be observable that  $\tilde{u}(x, t)$  is equal to:

$$\begin{aligned} \tilde{u}(x, t) &= - \int_0^x \left[ 1 - \cos \left( \frac{\partial \tilde{v}}{\partial r}(r, t) \right) \right] dr - \int_0^x \left[ 1 - \cos \left( \frac{\partial \tilde{w}}{\partial r}(r, t) \right) \right] dr \\ &= - \int_0^x \left[ 1 - \cos \left( \mathbf{\Phi}_y^T(r) \mathbf{q}_y(t) \right) \right] dr - \int_0^x \left[ 1 - \cos \left( \mathbf{\Phi}_z^T(r) \mathbf{q}_z(t) \right) \right] dr \end{aligned} \quad (19)$$

Eq. (19) can be rewritten by considering a second-order Taylor expansion, as follows:

$$\tilde{u}(x, t) \approx - \int_0^x \frac{\left( \mathbf{\Phi}_y^T(r) \mathbf{q}_y(t) \right)^2}{2} dr - \int_0^x \frac{\left( \mathbf{\Phi}_z^T(r) \mathbf{q}_z(t) \right)^2}{2} dr = - \frac{1}{2} \mathbf{q}^T(t) \mathbf{E}^{yz}(x) \mathbf{q}(t) \quad (20)$$

In Eq. (20),  $\mathbf{q}(t) = [\mathbf{q}_y^T(t), \mathbf{q}_z^T(t)]^T$  and  $\mathbf{E}^{yz}(x) = \text{diag}(\mathbf{E}_y(x), \mathbf{E}_z(x))$ , with  $\mathbf{E}_\bullet(x) = \int_0^x \Phi'_\bullet(r) \Phi_\bullet^T(r) dr$ . In addition, only one flexible mode is considered to model the traction-compression dynamics. Let  $\Delta u(t)$  be the overall deformation of the beam due to the axial load. Then, it follows that:

$$\Delta u(x, t) = \tau(x)\Delta u(t), \text{ with } \tau(x) = \frac{x}{l^{\mathcal{A}}} \quad (21)$$

Similarly, only one flexible mode is considered to represent the torsion dynamics due to transverse shear around the  $\mathbf{x}_a$ -axis. Let us now consider  $\Delta\phi(x, t)$  to be the axial angular deformation at any point of abscissa  $x$  ( $x \in [0, l^{\mathcal{A}}]$ ), which is caused by the axial torques  $\mathbf{W}_{\mathcal{A}/\bullet, P}\{4\}$  and  $\mathbf{W}_{\bullet/\mathcal{A}, C}\{4\}$ , applied by the beam  $\mathcal{A}$  at the point  $P$  and to the beam  $\mathcal{A}$  at the point  $C$ , respectively. Then, it is assumed that:

$$\Delta\phi(x, t) = \frac{x}{l^{\mathcal{A}}} (\phi_C^{\mathcal{A}}(t) - \phi_P^{\mathcal{A}}(t)) = \frac{x}{l^{\mathcal{A}}} \Delta\phi(t) = \sigma(x)\Delta\phi(t), \text{ with } \sigma(x) = \frac{x}{l^{\mathcal{A}}} \quad (22)$$

Let us also consider  $\mathbf{q}_f(t) = [\mathbf{q}_y^T(t), \mathbf{q}_z^T(t), \Delta u(t), \Delta\phi(t)]^T$  to be the vector (with  $2N + 2$  components) of all the internal elastic DOF of the body  $\mathcal{A}$  to be used in the LAGRANGE derivation (Eq. (3)). Then, Eq. (18) can be rewritten in the following way:

$$\mathbf{PM}(x, t) = \underbrace{\begin{bmatrix} x \\ 0 \\ 0 \end{bmatrix}}_{\mathbf{P}_0(x)} + \underbrace{\begin{bmatrix} \mathbf{0}_{1 \times N} & \mathbf{0}_{1 \times N} & \tau(x) & 0 \\ \Phi_y^T(x) & \mathbf{0}_{1 \times N} & 0 & 0 \\ \mathbf{0}_{1 \times N} & \Phi_z^T(x) & 0 & 0 \end{bmatrix}}_{\mathbf{M}_1^T(x)} \underbrace{\begin{bmatrix} \mathbf{q}_y(t) \\ \mathbf{q}_z(t) \\ \Delta u(t) \\ \Delta\phi(t) \end{bmatrix}}_{\mathbf{q}_f(t)} + \underbrace{\begin{bmatrix} -\frac{1}{2}\mathbf{q}_f^T(t) \begin{bmatrix} \mathbf{E}^{yz}(x) & \mathbf{0}_{2N \times 2} \\ \mathbf{0}_{2 \times 2N} & \mathbf{0}_{2 \times 2} \end{bmatrix} \mathbf{q}_f(t) \\ 0 \\ 0 \end{bmatrix}}_{\mathbf{P}_2(x, \mathbf{q}_f)} \quad (23)$$

Following the notation defined in Eq. (23), the inertial velocity  $\mathbf{v}_M^{\mathcal{A}}$  expressed in the frame  $\mathcal{R}_a$  is equal to:

$$\mathbf{v}_M^{\mathcal{A}} = \mathbf{v}_P^{\mathcal{A}} + \mathbf{M}_1^T(x)\dot{\mathbf{q}}_f(t) + \dot{\mathbf{P}}_2(x, \mathbf{q}_f) + (*\omega_P^{\mathcal{A}}) (\mathbf{P}_0(x) + \mathbf{M}_1^T(x)\mathbf{q}_f(t) + \mathbf{P}_2(x, \mathbf{q}_f)) \quad (24)$$

#### 4.2. Lagrangian computation and derivation

Let us define the overall vectors of quasi-coordinates  $\mathbf{Q}_p(t)$  and quasi-velocities  $\mathbf{Q}_v(t)$ , as well as their equilibrium values and variations:

$$\mathbf{Q}_p(t) = \begin{bmatrix} \mathbf{x}_P^{\mathcal{A}T}(t) & \Theta_P^{\mathcal{A}T}(t) & \mathbf{q}_f^T(t) \end{bmatrix}^T = \bar{\mathbf{Q}}_p + \delta\mathbf{Q}_p(t), \text{ with } \bar{\mathbf{Q}}_p = \begin{bmatrix} \bar{\mathbf{x}}_P^{\mathcal{A}T} & \bar{\Theta}_P^{\mathcal{A}T} & \mathbf{0}_{1 \times (2N+2)} \end{bmatrix}^T \quad (25)$$

$$\mathbf{Q}_v(t) = \begin{bmatrix} \mathbf{v}_P^{\mathcal{A}T}(t) & \omega_P^{\mathcal{A}T}(t) & \dot{\mathbf{q}}_f^T(t) \end{bmatrix}^T = \bar{\mathbf{Q}}_v + \delta\mathbf{Q}_v(t), \text{ with } \bar{\mathbf{Q}}_v = \begin{bmatrix} \bar{\mathbf{v}}_P^{\mathcal{A}T} & \bar{\omega}_P^{\mathcal{A}T} & \mathbf{0}_{1 \times (2N+2)} \end{bmatrix}^T \quad (26)$$

Indeed, according to the general assumptions, it is considered that  $\bar{\mathbf{q}}_f = \mathbf{0}_{(2N+2) \times 1}$ . The kinetic energy  $\mathcal{T}$  computation of the beam element  $\mathcal{A}$  can be outlined as follows:

$$\mathcal{T} = \frac{1}{2} \int_0^{l^{\mathcal{A}}} \rho^{\mathcal{A}} S^{\mathcal{A}} \mathbf{v}_M^{\mathcal{A}T} \mathbf{v}_M^{\mathcal{A}} dx + \underbrace{\frac{1}{2} \int_0^{l^{\mathcal{A}}} \rho^{\mathcal{A}} J_{px}^{\mathcal{A}} (\omega_P^{\mathcal{A}}\{1\} + \sigma(x)\Delta\dot{\phi}(t))^2 dx}_{\text{torsion contribution}} \quad (27)$$

By considering a second-order TAYLOR expansion of  $\mathcal{T}$  with respect to  $\delta\mathbf{Q}_p$  and  $\delta\mathbf{Q}_v$ , Eq. (27) can be expressed as:

$$\mathcal{T} = \frac{1}{2} \delta\mathbf{Q}_v^T(t) \mathbf{M}_{\mathcal{T}} \delta\mathbf{Q}_v(t) + \frac{1}{2} \delta\mathbf{Q}_p^T(t) \mathbf{K}_{\mathcal{T}} \delta\mathbf{Q}_p(t) + \frac{1}{2} \delta\mathbf{Q}_p^T(t) \mathbf{G}_{\mathcal{T}} \delta\mathbf{Q}_v(t) + \mathbf{C}_Q^T \delta\mathbf{Q}_v(t) + \mathbf{C}_Q^T \delta\mathbf{Q}_p(t) + \frac{1}{2} \bar{\mathbf{Q}}_v^T \mathbf{M}_{\mathcal{T}} \bar{\mathbf{Q}}_v \quad (28)$$

The kinetic energy of the beam does not depend on  $\bar{\mathbf{Q}}_p$ . However, the matrices  $\mathbf{K}_{\mathcal{T}}$  (the centrifugal stiffness matrix),  $\mathbf{G}_{\mathcal{T}}$ ,  $\mathbf{C}_Q$  and  $\mathbf{C}_Q$  are naturally dependent on  $\bar{\mathbf{Q}}_v$ . In addition, the calculation of the elastic potential energy, denoted as  $\mathcal{V}$ , consists of four distinct components:  $\mathcal{V}_b^y$ ,  $\mathcal{V}_b^z$ ,  $\mathcal{V}_t^x$  and  $\mathcal{V}_r^x$ . The terms  $\mathcal{V}_b^y$  and  $\mathcal{V}_b^z$  correspond to the elastic potential energy resulting from pure bending in the planes  $(P, \mathbf{x}_a, \mathbf{y}_a)$  and  $(P, \mathbf{x}_a, \mathbf{z}_a)$ , respectively, while  $\mathcal{V}_t^x$  and  $\mathcal{V}_r^x$  represent the contributions from the traction and torsion dynamics:

$$\left\{ \begin{array}{l} \mathcal{V}_b^y = \frac{1}{2} \mathbf{q}_y^T(t) \underbrace{\int_0^{l^{\mathcal{A}}} E^{\mathcal{A}} J_z^{\mathcal{A}} \Phi_y''(x) \Phi_y''^T(x) dx}_{\mathbf{K}_b^y} \mathbf{q}_y(t) \\ \mathcal{V}_b^z = \frac{1}{2} \mathbf{q}_z^T(t) \underbrace{\int_0^{l^{\mathcal{A}}} E^{\mathcal{A}} J_y^{\mathcal{A}} \Phi_z''(x) \Phi_z''^T(x) dx}_{\mathbf{K}_b^z} \mathbf{q}_z(t) \end{array} \right. \quad \left\{ \begin{array}{l} \mathcal{V}_t^x = \frac{1}{2} \Delta u(t) \underbrace{\int_0^{l^{\mathcal{A}}} E^{\mathcal{A}} S^{\mathcal{A}} \tau'(x) \tau'(x) dx}_{\mathbf{K}_t^x} \Delta u(t) \\ \mathcal{V}_r^x = \frac{1}{2} \Delta \phi(t) \underbrace{\int_0^{l^{\mathcal{A}}} G^{\mathcal{A}} J_{px}^{\mathcal{A}} \sigma'(x) \sigma'(x) dx}_{\mathbf{K}_r^x} \Delta \phi(t) \end{array} \right. , \quad (29)$$

with  $\mathcal{V} = \mathcal{V}_b^y + \mathcal{V}_b^z + \mathcal{V}_t^x + \mathcal{V}_r^x = \frac{1}{2} \delta \mathbf{Q}_p^T(t) \mathbf{K}_{\mathcal{V}} \delta \mathbf{Q}_p(t)$  and  $\mathbf{K}_{\mathcal{V}} = \text{diag}(\mathbf{0}_{6 \times 6}, \mathbf{K}_b^y, \mathbf{K}_b^z, \mathbf{K}_t^x, \mathbf{K}_r^x)$

The Lagrangian  $\mathcal{L} = \mathcal{T} - \mathcal{V}$  can ultimately be obtained and the LAGRANGE derivation (Eqs. (2) and (3)) leads to the following linear model:

$$\begin{aligned} \mathbf{M}_{\mathcal{T}} \delta \dot{\mathbf{Q}}_v(t) + \left[ \frac{1}{2} (\mathbf{G}_{\mathcal{T}}^T - \mathbf{G}_{\mathcal{T}}) + \begin{bmatrix} \mathbf{M}_{\mathcal{L}} \\ \mathbf{0}_{(2N+2) \times (6+2N+2)} \end{bmatrix} \right] \delta \mathbf{Q}_v(t) + \left[ \mathbf{K}_{\mathcal{V}} - \mathbf{K}_{\mathcal{T}} + \begin{bmatrix} \mathbf{J}_{\mathcal{L}} \\ \mathbf{0}_{(2N+2) \times (6+2N+2)} \end{bmatrix} \right] \delta \mathbf{Q}_p(t) \\ - \mathbf{C}_{\mathcal{Q}} + \begin{bmatrix} \mathbf{C}_{\mathcal{L}} \\ \mathbf{0}_{(2N+2) \times 1} \end{bmatrix} = \mathbf{W}_{\mathcal{L}}, \text{ with } \mathbf{W}_{\mathcal{L}} = \begin{bmatrix} \mathbf{F}_{\text{ext}/\mathcal{A},P} \\ \mathbf{T}_{\text{ext}/\mathcal{A},P} \\ \widehat{\mathbf{U}} \end{bmatrix} \end{aligned} \quad (30)$$

In Eq. (30), the matrices  $\mathbf{M}_{\mathcal{L}}$ ,  $\mathbf{J}_{\mathcal{L}}$  and  $\mathbf{C}_{\mathcal{L}}$  arise from the first-order approximation of the following term:

$$\left[ \begin{array}{cc} (*\omega_p^{\mathcal{A}}) & \mathbf{0}_3 \\ (*\mathbf{v}_p^{\mathcal{A}}) & (*\omega_p^{\mathcal{A}}) \end{array} \right] \frac{\partial \mathcal{L}}{\partial \left[ \begin{array}{c} \delta \mathbf{v}_p^{\mathcal{A}} \\ \delta \omega_p^{\mathcal{A}} \end{array} \right]} \quad (31)$$

The wrenches applied by the body  $\mathcal{A}$  and to the body  $\mathcal{A}$  are the interaction wrenches  $\mathbf{W}_{\mathcal{A}/\bullet,P}$  and  $\mathbf{W}_{\bullet/\mathcal{A},C}$  at the points  $P$  and  $C$ , respectively. Furthermore, the work of the external wrenches due to elastic deformations is equal to:

$$\mathcal{W}_{\text{ext}}(t) = \left[ \delta \mathbf{P} \mathbf{M}^T(l^{\mathcal{A}}, t) \quad \delta \Theta_{C/P}^T(l^{\mathcal{A}}, t) \right]^T \mathbf{W}_{\bullet/\mathcal{A},C}(t) \quad (32)$$

For the computation of the work, the distance vector  $\mathbf{P} \mathbf{M}(x, t)$  is detailed in Eq. (23). Additionally,  $\delta \Theta_{C/P}(x, t)$  represents the angular deformation of the point  $M(x)$  with respect to the equilibrium and it is given by  $\delta \Theta_{C/P}(x, t) = \left[ \Delta \phi(x, t), -\frac{\partial \bar{v}}{\partial x}^T(x, t), \frac{\partial \bar{v}}{\partial x}^T(x, t) \right]^T = \mathbf{M}_2^T(x) \mathbf{q}_f(t)$ , with:

$$\mathbf{M}_2^T(x) = \begin{bmatrix} \mathbf{0}_{1 \times N} & \mathbf{0}_{1 \times N} & 0 & \sigma(x) \\ \mathbf{0}_{1 \times N} & -\Phi_z^T(x) & 0 & 0 \\ \Phi_y^T(x) & \mathbf{0}_{1 \times N} & 0 & 0 \end{bmatrix} \quad (33)$$

Consequently, Eq. (32) becomes equal to:

$$\mathcal{W}_{\text{ext}}(t) = \left[ \mathbf{q}_f^T(t) \mathbf{M}_1(l^{\mathcal{A}}) + \mathbf{P}_2^T(l^{\mathcal{A}}, \mathbf{q}_f) \quad \mathbf{q}_f^T(t) \mathbf{M}_2(l^{\mathcal{A}}) \right] \mathbf{W}_{\bullet/\mathcal{A},C}(t) \quad (34)$$

By definition,  $\widehat{\mathbf{U}} = \frac{\partial \mathcal{W}_{\text{ext}}}{\partial \mathbf{q}_f}$ , meaning that the right-hand side of Eq. (30) reads:

$$\mathbf{W}_{\mathcal{L}} = \left[ \begin{array}{c} -\mathbf{I}_6 \\ \mathbf{0}_{(2N+2) \times 6} \end{array} \left[ \begin{array}{cc} \mathbf{M}_1(l^{\mathcal{A}}) + \frac{\partial \mathbf{P}_2^T(l^{\mathcal{A}}, \mathbf{q}_f)}{\partial \mathbf{q}_f} & \mathbf{M}_2(l^{\mathcal{A}}) \end{array} \right] \right] \left[ \begin{array}{c} \mathbf{W}_{\mathcal{A}/\bullet,P} \\ \mathbf{W}_{\bullet/\mathcal{A},C} \end{array} \right] = \mathbf{N} \left[ \begin{array}{c} \mathbf{W}_{\mathcal{A}/\bullet,P} \\ \mathbf{W}_{\bullet/\mathcal{A},C} \end{array} \right] \quad (35)$$

### 4.3. Equilibrium conditions

Taking into account the assumptions that have been made, this approach is only valid in the proximity of the equilibrium point that is characterized by  $\bar{\mathbf{q}}_f = \mathbf{0}_{(2N+2) \times 1}$ . Therefore, it is essential to verify that these conditions are satisfied. This task can be accomplished by employing Eqs. (30) and (35) to derive the subsequent equilibrium:

$$\left[ \mathbf{K}_{\mathcal{V}} - \mathbf{K}_{\mathcal{T}} + \begin{bmatrix} \mathbf{J}_{\mathcal{L}} \\ \mathbf{0}_{(2N+2) \times (6+2N+2)} \end{bmatrix} \right] \begin{bmatrix} \star \\ \bar{\mathbf{q}}_f \end{bmatrix} - \mathbf{C}_{\mathcal{Q}} + \begin{bmatrix} \mathbf{C}_{\mathcal{L}} \\ \mathbf{0}_{(2N+2) \times 1} \end{bmatrix} = \bar{\mathbf{N}} \begin{bmatrix} \bar{\mathbf{W}}_{\mathcal{A}/\bullet, P} \\ \bar{\mathbf{W}}_{\bullet/\mathcal{A}, C} \end{bmatrix} \quad (36)$$

Indeed, the geometric equilibrium conditions  $\left[ \bar{\mathbf{x}}_P^{\mathcal{A}^T}, \bar{\boldsymbol{\Theta}}_P^{\mathcal{A}^T} \right]^T$  are always multiplied by null terms in the equilibrium computation displayed in Eq. (36). For this reason, they do not have to be taken into account. By means of Eq. (36),  $\bar{\mathbf{W}}_{\mathcal{A}/\bullet, P}$  and  $\bar{\mathbf{q}}_f$  can be calculated from  $\bar{\mathbf{W}}_{\bullet/\mathcal{A}, C}$ , making it possible to confirm all the assumptions. After verifying all the hypotheses,  $\bar{\mathbf{W}}_{\mathcal{A}/\bullet, P}$  can be recomputed with the help of the following equation:

$$-\mathbf{C}_{\mathcal{Q}} + \begin{bmatrix} \mathbf{C}_{\mathcal{L}} \\ \mathbf{0}_{(2N+2) \times 1} \end{bmatrix} = \bar{\mathbf{N}} \begin{bmatrix} \bar{\mathbf{W}}_{\mathcal{A}/\bullet, P} \\ \bar{\mathbf{W}}_{\bullet/\mathcal{A}, C} \end{bmatrix} \quad (37)$$

Let us now consider a simple scenario involving a beam with a tip mass. This beam is attached to a spinning rigid hub with radius  $r$ , as displayed in Fig. 6a. In this case, the centrifugal force with magnitude  $\bar{\mathbf{W}}_{\bullet/\mathcal{A}, C}\{1\}$  which arises from the spinning motion is equal to  $\bar{\mathbf{W}}_{\bullet/\mathcal{A}, C}\{1\} = m(l^{\mathcal{A}} + r)\Omega^2$ , where  $m$  is the tip mass value located at the point  $C$  and  $l^{\mathcal{A}}$  represents the length of the beam. In this scenario,  $\bar{\mathbf{x}}_P^{\mathcal{A}} = [r, 0, 0]^T$ ,  $\bar{\boldsymbol{\Theta}}_P^{\mathcal{A}} = \mathbf{0}_{3 \times 1}$  and  $\bar{\boldsymbol{\omega}}_P^{\mathcal{A}} = [0, 0, \Omega]^T$ . For this reason, it can be concluded that  $\bar{\mathbf{W}}_{\bullet/\mathcal{A}, C} = [m(l^{\mathcal{A}} + r)\Omega^2, 0, 0, 0, 0, 0]^T$ . Due to the spinning motion, it can also be inferred that  $\bar{\mathbf{v}}_P^{\mathcal{A}} = [0, r\Omega, 0]^T$ . These equilibrium conditions are expressed in the body frame  $\mathcal{R}_a$ , which is the frame of reference used to define the beam model. A similar procedure can be carried out for the computation of  $\bar{\mathbf{v}}_C^{\mathcal{A}}$ , with  $\bar{\mathbf{v}}_C^{\mathcal{A}} = [0, (l^{\mathcal{A}} + r)\Omega, 0]^T$ . However,  $\bar{\mathbf{v}}_C^{\mathcal{A}}$  does not parameterize the beam model and is only relevant if another body is attached to the beam at the point  $C$ . This scenario occurs when a tip mass is present but also when two different beams are connected in series, as displayed in Fig. 6b.

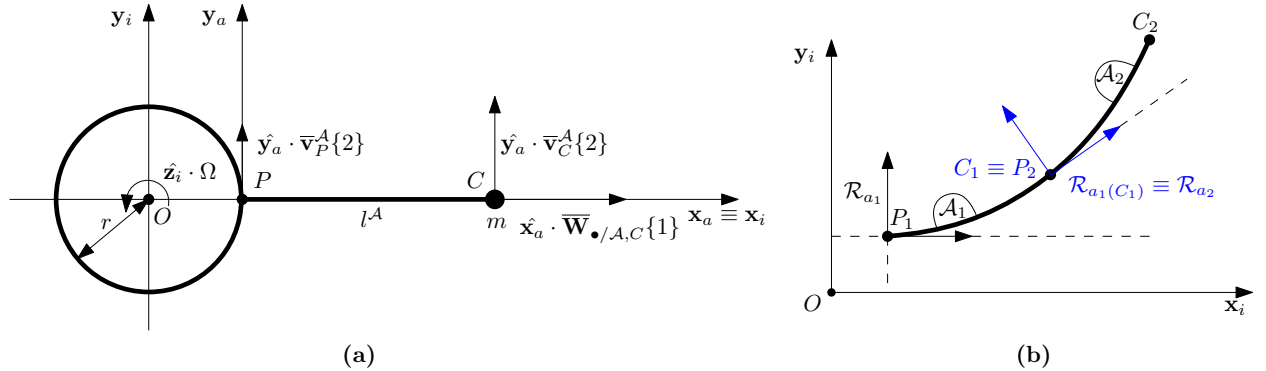


Figure 6: (a) Scenario where a beam with length  $l^{\mathcal{A}}$  is connected to a spinning rigid hub at the point  $P$  and to a tip mass at the point  $C$ : this figure provides a geometrical interpretation of how the inertial velocity and force components in equilibrium are expressed in  $\mathcal{R}_a$  with respect to the configuration of the system. (b) Assembly of two flexible rotating beams in series.

### 4.4. Assembly of beams with other substructures

When the beam  $\mathcal{A}$  is connected to another body  $\bullet$  at the point  $C$ , one has to take into account the projection in the deformed body frame  $\mathcal{R}_{a(C)}$  of the interaction wrench  $\mathbf{W}_{\bullet/\mathcal{A}, C}$ , as illustrated in Fig. 6b with the connection of two flexible beams in series: the frames  $\mathcal{R}_{a_1(C_1)}$  and  $\mathcal{R}_{a_2}$  are coincident. Therefore, the DCM  $\mathbf{P}_{\mathcal{R}_{a(C)}/\mathcal{R}_a}$  between the frames  $\mathcal{R}_{a(C)}$  and  $\mathcal{R}_a$  is introduced, such that:

$$[\mathbf{W}_{\bullet/\mathcal{A},C}]_{\mathcal{R}_a} = \mathbf{P}_{\mathcal{R}_{a(C)}/\mathcal{R}_a}^{\times 2} [\mathbf{W}_{\bullet/\mathcal{A},C}]_{\mathcal{R}_{a(C)}} \quad (38)$$

This DCM is given by the following first-order approximation:

$$\mathbf{P}_{\mathcal{R}_{a(C)}/\mathcal{R}_a} = \begin{bmatrix} 1 & -\Phi_y^T(l^{\mathcal{A}})\mathbf{q}_y(t) & -\Phi_z^T(l^{\mathcal{A}})\mathbf{q}_z(t) \\ \Phi_y^T(l^{\mathcal{A}})\mathbf{q}_y(t) & 1 & -\sigma(l^{\mathcal{A}})\Delta\phi(t) \\ \Phi_z^T(l^{\mathcal{A}})\mathbf{q}_z(t) & \sigma(l^{\mathcal{A}})\Delta\phi(t) & 1 \end{bmatrix} \quad (39)$$

Therefore, the linearization of Eq. (38) leads to  $[\overline{\mathbf{W}}_{\bullet/\mathcal{A},C}]_{\mathcal{R}_a} = [\overline{\mathbf{W}}_{\bullet/\mathcal{A},C}]_{\mathcal{R}_{a(C)}}$  and also to:

$$[\delta\mathbf{W}_{\bullet/\mathcal{A},C}]_{\mathcal{R}_a} = [\delta\mathbf{W}_{\bullet/\mathcal{A},C}]_{\mathcal{R}_{a(C)}} + \underbrace{\begin{bmatrix} -\Phi_y^T(l^{\mathcal{A}})\overline{\mathbf{W}}_{\bullet/\mathcal{A},C}\{2\} & -\Phi_z^T(l^{\mathcal{A}})\overline{\mathbf{W}}_{\bullet/\mathcal{A},C}\{3\} & 0 & 0 \\ \Phi_y^T(l^{\mathcal{A}})\overline{\mathbf{W}}_{\bullet/\mathcal{A},C}\{1\} & \mathbf{0}_{1 \times N} & 0 & -\sigma(l^{\mathcal{A}})\overline{\mathbf{W}}_{\bullet/\mathcal{A},C}\{3\} \\ \mathbf{0}_{1 \times N} & \Phi_z^T(l^{\mathcal{A}})\overline{\mathbf{W}}_{\bullet/\mathcal{A},C}\{1\} & 0 & \sigma(l^{\mathcal{A}})\overline{\mathbf{W}}_{\bullet/\mathcal{A},C}\{2\} \\ -\Phi_y^T(l^{\mathcal{A}})\overline{\mathbf{W}}_{\bullet/\mathcal{A},C}\{5\} & -\Phi_z^T(l^{\mathcal{A}})\overline{\mathbf{W}}_{\bullet/\mathcal{A},C}\{6\} & 0 & 0 \\ \Phi_y^T(l^{\mathcal{A}})\overline{\mathbf{W}}_{\bullet/\mathcal{A},C}\{4\} & \mathbf{0}_{1 \times N} & 0 & -\sigma(l^{\mathcal{A}})\overline{\mathbf{W}}_{\bullet/\mathcal{A},C}\{6\} \\ \mathbf{0}_{1 \times N} & \Phi_z^T(l^{\mathcal{A}})\overline{\mathbf{W}}_{\bullet/\mathcal{A},C}\{4\} & 0 & \sigma(l^{\mathcal{A}})\overline{\mathbf{W}}_{\bullet/\mathcal{A},C}\{5\} \end{bmatrix}}_{\mathbf{W}_C} \mathbf{q}_f(t) \quad (40)$$

As previously mentioned, the ultimate goal is to establish a linear model for the rotating beam  $\mathcal{A}$  around a specific equilibrium point. For this reason, only the first-order terms originating from the TAYLOR series expansion of  $\mathbf{W}_{\mathcal{L}}$  are taken into consideration. Subsequently, all the various quantities are approximated as the sum of their equilibrium values and slight deviations from these values. A first-order linearization is finally applied to Eqs. (30) and (35). Furthermore, the expression of  $[\delta\mathbf{W}_{\bullet/\mathcal{A},C}]_{\mathcal{R}_a}$  displayed in Eq. (40) is taken into account in this linearization, leading to the following linearized Lagrangian derivation of the spinning beam:

$$\mathbf{M}_{\mathcal{T}}\delta\dot{\mathbf{Q}}_v(t) + \left[ \frac{1}{2}(\mathbf{G}_{\mathcal{T}}^T - \mathbf{G}_{\mathcal{T}}) + \begin{bmatrix} \mathbf{M}_{\mathcal{L}} \\ \mathbf{0}_{(2N+2) \times (6+2N+2)} \end{bmatrix} \right] \delta\mathbf{Q}_v(t) + \left[ \mathbf{K}_{\mathcal{V}} - \mathbf{K}_{\mathcal{T}} + \begin{bmatrix} \mathbf{J}_{\mathcal{L}} \\ \mathbf{0}_{(2N+2) \times (6+2N+2)} \end{bmatrix} + \mathbf{F}_c \right] \delta\mathbf{Q}_p(t) = \overline{\mathbf{N}} \begin{bmatrix} [\delta\mathbf{W}_{\mathcal{A}/\bullet,P}]_{\mathcal{R}_a} \\ [\delta\mathbf{W}_{\bullet/\mathcal{A},C}]_{\mathcal{R}_{a(C)}} \end{bmatrix} \quad (41)$$

In Eq. (41), the additional stiffness matrix  $\mathbf{F}_c$  depends on  $\overline{\mathbf{W}}_{\bullet/\mathcal{A},C}$  due to the matrices  $\mathbf{W}_C$  (in Eq. (40)) and  $\mathbf{N}$  (in Eq. (35)). It can also be noticed that all the constant terms which were present in Eq. (30) cancelled out. Ultimately, Eq. (41) can be rewritten as:

$$\begin{bmatrix} \mathbf{M}_{rr} & \mathbf{M}_{rf} \\ \mathbf{M}_{fr} & \mathbf{M}_{ff} \end{bmatrix} \begin{bmatrix} \frac{\delta\dot{\mathbf{v}}_p^{\mathcal{A}}}{\delta\dot{\omega}_p^{\mathcal{A}}} \\ \dot{\mathbf{q}}_f(t) \end{bmatrix}_{\mathcal{R}_a} + \begin{bmatrix} \mathbf{D}_{rr} & \mathbf{D}_{rf} \\ \mathbf{D}_{fr} & \mathbf{D}_{ff} \end{bmatrix} \begin{bmatrix} \frac{\delta\mathbf{v}_p^{\mathcal{A}}}{\delta\omega_p^{\mathcal{A}}} \\ \dot{\mathbf{q}}_f(t) \end{bmatrix}_{\mathcal{R}_a} + \begin{bmatrix} \mathbf{K}_{rr} & \mathbf{K}_{rf} \\ \mathbf{K}_{fr} & \mathbf{K}_{ff} \end{bmatrix} \begin{bmatrix} \frac{\delta\mathbf{x}_p^{\mathcal{A}}}{\delta\boldsymbol{\Theta}_p^{\mathcal{A}}} \\ \mathbf{q}_f(t) \end{bmatrix}_{\mathcal{R}_a} = \begin{bmatrix} \overline{\mathbf{N}}_{rr} & \overline{\mathbf{N}}_{rf} \\ \overline{\mathbf{N}}_{fr} & \overline{\mathbf{N}}_{ff} \end{bmatrix} \begin{bmatrix} [\delta\mathbf{W}_{\mathcal{A}/\bullet,P}]_{\mathcal{R}_a} \\ [\delta\mathbf{W}_{\bullet/\mathcal{A},C}]_{\mathcal{R}_{a(C)}} \end{bmatrix} \quad (42)$$

#### 4.5. TITOP model of a flexible spinning beam

Before deriving the state-space representation of the TITOP beam model, it is essential to compute the output motion vector of the beam at the point  $C$ . First, it can be deduced that:

$$\mathbf{x}_C^{\mathcal{A}} = \mathbf{OP} + \mathbf{PC} = \mathbf{x}_P^{\mathcal{A}} + \mathbf{PC} \quad (43)$$

The computation of  $\mathbf{PC}$  is given by Eq. (23), with  $x = l^{\mathcal{A}}$ . Furthermore, it can be observed from Fig. 5, the first spatial derivative of Eq. (16) and Eq. (22) that:

$$\Theta_C^{\mathcal{A}} = \Theta_P^{\mathcal{A}} + \delta\Theta_{C/P}(l^{\mathcal{A}}, t) = \Theta_P^{\mathcal{A}} + \mathbf{M}_2^T(l^{\mathcal{A}})\mathbf{q}_f \quad (44)$$

For the computation of the inertial velocity vector  $\mathbf{v}_C^{\mathcal{A}}$ , an equivalent approach to the one employed in Eq. (17) is used, with:

$$\mathbf{v}_C^{\mathcal{A}} = \mathbf{v}_P^{\mathcal{A}} + \left. \frac{d\mathbf{PC}}{dt} \right|_{\mathcal{R}_a} + \omega_P^{\mathcal{A}} \wedge \mathbf{PC} \quad (45)$$

For the computation of the angular velocity vector at the point C, it is crucial to emphasize that  $\omega_C^{\mathcal{A}}$  is equivalent to  $\omega_{\mathcal{R}_{a(C)}/\mathcal{R}_i}$ , which represents the angular velocity vector of the deformed body frame  $\mathcal{R}_{a(C)}$  at the point C with respect to the inertial frame  $\mathcal{R}_i$ . On that account, it follows that:

$$\omega_C^{\mathcal{A}} = \omega_{\mathcal{R}_{a(C)}/\mathcal{R}_a} + \omega_{\mathcal{R}_a/\mathcal{R}_i} = \mathbf{M}_2^T(l^{\mathcal{A}})\dot{\mathbf{q}}_f + \omega_P^{\mathcal{A}} \quad (46)$$

Ultimately, the computation of the acceleration vectors  $\dot{\mathbf{v}}_C^{\mathcal{A}}$  and  $\dot{\omega}_C^{\mathcal{A}}$  can directly be obtained by applying a time derivation to Eqs. (45) and (46), respectively. Eqs. (43), (44), (45) and (46) are projected in the body frame of the beam, denoted as  $\mathcal{R}_a$ . However, the output motion vector computed at the point C also needs to be projected in the beam's deformed body frame  $\mathcal{R}_{a(C)}$ . The need for this projection is driven by the same reasons that prompted the projection of the input computations  $\mathbf{W}_{\bullet/\mathcal{A},C}$  into  $\mathcal{R}_{a(C)}$ , with:

$$\left[ \mathbf{m}_C^{\mathcal{A}} \right]_{\mathcal{R}_{a(C)}} = \mathbf{P}_{\mathcal{R}_a/\mathcal{R}_{a(C)}}^{\times 6} \left[ \mathbf{m}_C^{\mathcal{A}} \right]_{\mathcal{R}_a} \quad (47)$$

Subsequently, Eqs. (43), (44), (45) and (46), along with the time derivations of Eqs. (45) and (46), are incorporated into Eq. (47), which is thereafter subjected to a first-order linearization. This process yields the computation of the output motion vector, as follows:

$$\left[ \delta\mathbf{m}_C^{\mathcal{A}} \right]_{\mathcal{R}_{a(C)}} = \left[ \mathbf{M}_l \mid \mathbf{M}_r \right] \left[ \begin{array}{c} \delta\dot{\mathbf{v}}_P^{\mathcal{A}} \\ \delta\dot{\omega}_P^{\mathcal{A}} \\ \dot{\mathbf{q}}_f(t) \end{array} \right]_{\mathcal{R}_a} + \left[ \mathbf{D}_l \mid \mathbf{D}_r \right] \left[ \begin{array}{c} \delta\mathbf{v}_P^{\mathcal{A}} \\ \delta\omega_P^{\mathcal{A}} \\ \dot{\mathbf{q}}_f(t) \end{array} \right]_{\mathcal{R}_a} + \left[ \mathbf{K}_l \mid \mathbf{K}_r \right] \left[ \begin{array}{c} \delta\mathbf{x}_P^{\mathcal{A}} \\ \delta\Theta_P^{\mathcal{A}} \\ \mathbf{q}_f(t) \end{array} \right]_{\mathcal{R}_a} \quad (48)$$

Finally, Eqs. (42) and (48) can be transformed into a state-space representation of the linearized two-port beam model  $\left[ \mathfrak{X}_{PC}^{\mathcal{A}}(s) \right]_{\mathcal{R}_{a(C)}}$ , as follows:

$$\left[ \begin{array}{c} \dot{\mathbf{q}}_f(t) \\ \ddot{\mathbf{q}}_f(t) \\ \left[ \delta\mathbf{m}_C^{\mathcal{A}} \right]_{\mathcal{R}_{a(C)}} \\ \left[ \delta\mathbf{W}_{\mathcal{A}/\bullet,P} \right]_{\mathcal{R}_a} \end{array} \right]_{\mathcal{R}_{a(C)}} = \left[ \begin{array}{c|c} \mathbf{A} & \mathbf{B} \\ \hline \mathbf{C} & \mathbf{D} \end{array} \right] \left[ \begin{array}{c} \mathbf{q}_f(t) \\ \dot{\mathbf{q}}_f(t) \\ \left[ \delta\mathbf{W}_{\bullet/\mathcal{A},C} \right]_{\mathcal{R}_{a(C)}} \\ \left[ \delta\mathbf{m}_P^{\mathcal{A}} \right]_{\mathcal{R}_a} \end{array} \right] \quad (49)$$

In Eq. (49), the matrices  $\mathbf{A}$ ,  $\mathbf{B}$ ,  $\mathbf{C}$  and  $\mathbf{D}$  are given by:

$$\begin{aligned} \mathbf{A} &= \left[ \begin{array}{cc} \mathbf{0}_{(2N+2) \times (2N+2)} & \mathbf{I}_{(2N+2)} \\ -\mathbf{M}_{ff}^{-1} \mathbf{K}_{ff} & -\mathbf{M}_{ff}^{-1} \mathbf{D}_{ff} \end{array} \right]_{\mathcal{R}_a} \\ \mathbf{B} &= \left[ \begin{array}{cc} \mathbf{0}_{(2N+2) \times 6} & \mathbf{0}_{(2N+2) \times 18} \\ \mathbf{M}_{ff}^{-1} \bar{\mathbf{N}}_{ff} & -\mathbf{M}_{ff}^{-1} \left[ \mathbf{M}_{fr} \quad \mathbf{D}_{fr} \quad \mathbf{K}_{fr} \right] \end{array} \right]_{\mathcal{R}_a} \\ \mathbf{C} &= \left[ \begin{array}{cc} -\mathbf{M}_r \mathbf{M}_{ff}^{-1} \mathbf{K}_{ff} + \mathbf{K}_r & -\mathbf{M}_r \mathbf{M}_{ff}^{-1} \mathbf{D}_{ff} + \mathbf{D}_r \\ -(\bar{\mathbf{N}}_{rr})^{-1} (\mathbf{M}_{rf} \mathbf{M}_{ff}^{-1} \mathbf{K}_{ff} - \mathbf{K}_{rf}) & -(\bar{\mathbf{N}}_{rr})^{-1} (\mathbf{M}_{rf} \mathbf{M}_{ff}^{-1} \mathbf{D}_{ff} - \mathbf{D}_{rf}) \end{array} \right]_{\mathcal{R}_a} \\ \mathbf{D} &= \left[ \begin{array}{cc} \mathbf{M}_r \mathbf{M}_{ff}^{-1} \bar{\mathbf{N}}_{ff} & -\mathbf{M}_r \mathbf{M}_{ff}^{-1} \left[ \mathbf{M}_{fr} \quad \mathbf{D}_{fr} \quad \mathbf{K}_{fr} \right] + \left[ \mathbf{M}_l \quad \mathbf{D}_l \quad \mathbf{K}_l \right] \\ (\bar{\mathbf{N}}_{rr})^{-1} (\mathbf{M}_{rf} \mathbf{M}_{ff}^{-1} \bar{\mathbf{N}}_{ff} - \bar{\mathbf{N}}_{rf}) & (\bar{\mathbf{N}}_{rr})^{-1} \left[ \mathbf{M}_{rr} \quad \mathbf{D}_{rr} \quad \mathbf{K}_{rr} \right] - (\bar{\mathbf{N}}_{rr})^{-1} \mathbf{M}_{rf} \mathbf{M}_{ff}^{-1} \left[ \mathbf{M}_{fr} \quad \mathbf{D}_{fr} \quad \mathbf{K}_{fr} \right] \end{array} \right]_{\mathcal{R}_a} \end{aligned} \quad (50)$$

All the matrices which are employed in this section to build the model of the spinning beam are defined in [Appendix B](#). In addition, a summary of all the steps that need to be followed to compute the state-space representation of the TITOP beam model is also depicted in [Algorithm 1](#).

---

**Algorithm 1:** Computation of the TITOP beam model
 

---

Define the beam's mechanical parameters:  $\rho^{\mathcal{A}}, S^{\mathcal{A}}, I^{\mathcal{A}}, E^{\mathcal{A}}, \nu^{\mathcal{A}}, G^{\mathcal{A}}, J_{px}^{\mathcal{A}}, J_y^{\mathcal{A}}$  and  $J_z^{\mathcal{A}}$ ;  
 Define the equilibrium conditions:  $\bar{\mathbf{x}}_P^{\mathcal{A}}, \bar{\mathbf{v}}_P^{\mathcal{A}}, \bar{\boldsymbol{\omega}}_P^{\mathcal{A}}$  and  $\bar{\mathbf{W}}_{\bullet/\mathcal{A},C}$ ;  
 Compute  $\mathbf{M}_{\mathcal{T}}, \mathbf{K}_{\mathcal{T}}, \mathbf{G}_{\mathcal{T}}, \mathbf{K}_{\mathcal{V}}, \mathbf{C}_{\mathcal{Q}}, \mathbf{M}_{\mathcal{L}}, \mathbf{J}_{\mathcal{L}}, \mathbf{C}_{\mathcal{L}}$  and  $\bar{\mathbf{N}}$ ; ▷ see [Appendix B](#)  
 Compute  $\bar{\mathbf{W}}_{\mathcal{A}/\bullet,P}$  and  $\bar{\mathbf{q}}_f$  from the equilibrium equations; ▷ see Eq. (36)  
**if**  $\bar{\mathbf{q}}_f \gg \mathbf{0}_{(2N+2) \times 1}$  **then**  
 | The model is not valid;  
**else**  
 | Compute  $\mathbf{F}_c$ , as well as the Lagrangian derivation; ▷ see [Appendix B](#) and Eq. (41)  
 | Compute  $\mathbf{M}_l, \mathbf{M}_r, \mathbf{D}_l, \mathbf{D}_r, \mathbf{K}_l$  and  $\mathbf{K}_r$ ; ▷ see [Appendix B](#)  
 | Compute the TITOP beam model; ▷ see Eqs. (49) and (50)  
**end**

---

## 5. Model Validation

### 5.1. Frequency ratios of a spinning beam with tip mass and root offset

The simple scenario presented in Fig. 6a involving a beam with a tip mass is considered in order to validate the TITOP model of a flexible spinning beam. The following parameters are used in this section: the rotation speed ratios  $\eta_{\bullet}^{\star}$ , which are defined differently for the four different types of dynamics, the dimensionless tip mass  $\mu = \frac{m}{\rho^{\mathcal{A}} S^{\mathcal{A}} l^{\mathcal{A}}}$  and the dimensionless hub radius  $\alpha = \frac{r}{l^{\mathcal{A}}}$ . The rotation speed ratios  $\eta_{\bullet}^{\star}$  are equal to  $\eta_b^y = \Omega \sqrt{\frac{\rho^{\mathcal{A}} S^{\mathcal{A}} I^{\mathcal{A}4}}{E^{\mathcal{A}} J_z^{\mathcal{A}}}}$  for in-plane bending (i.e., in the plane  $(P, \mathbf{x}_a, \mathbf{y}_a)$ ),  $\eta_b^z = \Omega \sqrt{\frac{\rho^{\mathcal{A}} S^{\mathcal{A}} I^{\mathcal{A}4}}{E^{\mathcal{A}} J_y^{\mathcal{A}}}}$  for out-of-plane bending (i.e., in the plane  $(P, \mathbf{x}_a, \mathbf{z}_a)$ ),  $\eta_t^x = \Omega \sqrt{\frac{\rho^{\mathcal{A}} I^{\mathcal{A}2}}{E^{\mathcal{A}}}}$  for traction and  $\eta_r^x = \Omega \sqrt{\frac{\rho^{\mathcal{A}} I^{\mathcal{A}2}}{G^{\mathcal{A}}}}$  for torsion. A variety of results is tabulated for general use in Tables 1, 2 and 3, which considers uniform beams with fixed root boundary conditions for different values of tip mass, root offset and angular velocity  $\Omega$ . To generate these tables, the model displayed in Fig. 7 is considered. This model involves a beam  $\mathcal{A}$  connected to a tip mass  $\mathcal{S}$ , where the beam is clamped at the point  $P$  to a massless rotor. The procedure for determining the equilibrium conditions in the beam model is similar to the one illustrated in Fig. 6a and explained in section 4, since it is once again assumed that  $\bar{\mathbf{x}}_P^{\mathcal{A}} = [r, 0, 0]^T$ ,  $\bar{\boldsymbol{\Theta}}_P^{\mathcal{A}} = \mathbf{0}_{3 \times 1}$  and  $\bar{\boldsymbol{\omega}}_P^{\mathcal{A}} = [0, 0, \Omega]^T$ . Finally, it is also considered that  $\mathbf{P}_{\mathcal{R}_s/\mathcal{R}_{a(C)}} = \mathbf{I}_3$  and  $m = m^{\mathcal{S}}$ .

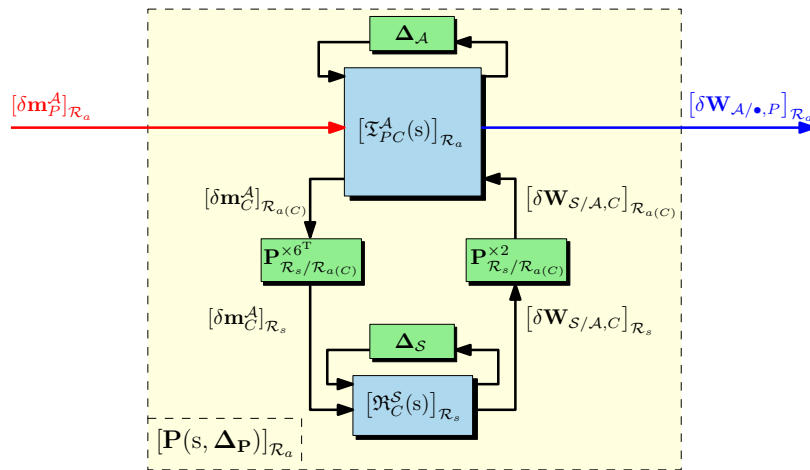


Figure 7: Block-diagram representation of a model composed of a flexible beam and a tip mass.

Given that Tables 1, 2 and 3 present dimensionless results, it is crucial to emphasize that different combinations of beam parameters, such as length and Young's modulus, must yield identical frequency ratios to those depicted in the tables. However, the choice of beam parameters and rotation speed ratios, denoted as  $\eta_\bullet^*$ , can lead to situations where the resulting  $\Omega$  may challenge the validity of the beam model. This can be explained by the fact that it could lead to scenarios in which the beam's deformation assumptions no longer hold. For the specific scenario presented here, the geometrical configuration displayed in Fig. 6a is being considered. For this reason,  $\overline{\mathbf{W}}_{S/\mathcal{A},C} = [m^S (l^{\mathcal{A}} + r) \Omega^2, 0, 0, 0, 0, 0]^T$ . Since  $\overline{\mathbf{W}}_{S/\mathcal{A},C}\{1\} \neq 0$ , very big values of  $\Omega$  and  $m^S$  might lead to  $\overline{\Delta u} \gg 0$ , depending on the chosen beam parameters, which would invalidate the beam model.

One of the objectives of this paper is also to demonstrate how to model a system parameterized according to the angular velocity  $\Omega$ . Therefore,  $\Omega$  is considered as an uncertain parameter, as follows:

$$\Omega = \Omega_0(1 + r_\Omega \delta_\Omega) \quad (51)$$

In Eq. (51),  $\Omega_0$  represents the nominal angular velocity,  $r_\Omega$  is used to set the maximum percent of variation for  $\Omega$  and  $\delta_\Omega \in [-1, 1]$  is a normalized real uncertainty. The mass of the body  $\mathcal{S}$  (tip mass) can also be considered uncertain, with  $m^S = m_0^S(1 + r_{m^S} \delta_{m^S})$ . Therefore, the structured uncertainty blocks (displayed in Fig. 7) characterizing the flexible boom and the tip mass are equal to  $\Delta_{\mathcal{A}} = \text{diag}(\delta_\Omega \mathbf{I}_{169}, \delta_{m^S} \mathbf{I}_{64})$  and  $\Delta_{\mathcal{S}} = \text{diag}(\delta_\Omega \mathbf{I}_4, \delta_{m^S} \mathbf{I}_5)$ , respectively. Lastly, it should also be noted that the number of computed occurrences for the different uncertainties depends on the equilibrium conditions computation of the system.

Table 1: Frequency ratios of a uniform cantilever beam with zero root offset and zero tip mass;  $\alpha = 0, \mu = 0$ .

Frequency ratios of the flexible modes										
$\eta_\bullet^*$	In-plane bending				Out-of-plane bending				Traction	Torsion
	1 <sup>st</sup>	2 <sup>nd</sup>	3 <sup>rd</sup>	4 <sup>th</sup>	1 <sup>st</sup>	2 <sup>nd</sup>	3 <sup>rd</sup>	4 <sup>th</sup>	1 <sup>st</sup>	1 <sup>st</sup>
0	3.5160	22.1578	63.3466	281.5963	3.5160	22.1578	63.3466	281.5963	1732	1719
2	3.6218	22.6384	63.8495	281.7849	4.1373	22.7266	63.8809	281.7920	1732	1719
4	3.8978	24.0256	65.3351	282.3501	5.5852	24.3564	65.4575	282.3785	1732	1719
6	4.2643	26.1815	67.7383	283.2900	7.3614	26.8602	68.0035	283.3535	1732	1719
8	4.6626	28.9382	70.9651	284.6012	9.2602	30.0237	71.4147	284.7137	1732	1719
10	5.0653	32.1424	74.9079	286.2793	11.2106	33.6622	75.5725	286.4540	1732	1719

Table 2: Frequency ratios of a uniform cantilever beam with zero tip mass;  $\alpha = 1, \mu = 0$ .

Frequency ratios of the flexible modes										
$\eta_\bullet^*$	In-plane bending				Out-of-plane bending				Traction	Torsion
	1 <sup>st</sup>	2 <sup>nd</sup>	3 <sup>rd</sup>	4 <sup>th</sup>	1 <sup>st</sup>	2 <sup>nd</sup>	3 <sup>rd</sup>	4 <sup>th</sup>	1 <sup>st</sup>	1 <sup>st</sup>
0	3.5160	22.1578	63.3466	281.5963	3.5160	22.1578	63.3466	281.5963	1732	1719
2	4.4006	23.3799	64.5881	282.0294	4.8339	23.4653	64.6190	282.0365	1732	1719
4	6.3165	26.7142	68.1767	283.3255	7.4768	27.0120	68.2939	283.3538	1732	1719
6	8.5561	31.4937	73.7678	285.4753	10.4513	32.0602	74.0115	285.5384	1732	1719
8	10.9044	37.1564	80.9404	288.4635	13.5265	38.0080	81.3349	288.5745	1732	1719
10	13.2997	43.3492	89.3024	292.2694	16.6442	44.4878	89.8606	292.4405	1732	1719

## 5.2. Comparison with other solutions and NASTRAN

It is also very useful and important to compare the results obtained from the TITOP methodology presented in this paper with other solutions, as well as the results of a conventional finite element code. Table 4 provides such a comparison for the simple case of a uniform cantilever beam with no root offset or tip mass, where  $f_{b,\bullet}^z$  and  $f_{b,\bullet}^y$  represent the out-of-plane and in-plane frequency ratios, respectively. The method of Frobenius is employed to determine the exact out-of-plane frequencies for rotating beams, where both the flexural rigidity and mass distribution

Table 3: Frequency ratios of a uniform cantilever beam with zero root offset;  $\alpha = 0, \mu = 1$ .

$\eta_b^*$	Frequency ratios of the flexible modes									
	In-plane bending				Out-of-plane bending				Traction	Torsion
	1 <sup>st</sup>	2 <sup>nd</sup>	3 <sup>rd</sup>	4 <sup>th</sup>	1 <sup>st</sup>	2 <sup>nd</sup>	3 <sup>rd</sup>	4 <sup>th</sup>	1 <sup>st</sup>	1 <sup>st</sup>
0	1.5573	16.2709	51.6537	184.8364	1.5573	16.2709	51.6537	184.8364	866.03	1719
2	1.7682	18.0920	53.7584	186.4674	2.6697	18.2022	53.7956	186.4781	866.03	1719
4	2.1544	22.6744	59.6400	191.2771	4.5435	23.0245	59.7740	191.3189	866.05	1719
6	2.5325	28.6878	68.3475	199.0362	6.5132	29.3086	68.6104	199.1266	866.09	1719
8	2.8898	35.3872	78.9597	209.4181	8.5070	36.2802	79.3640	209.5709	866.14	1719
10	3.2380	42.4412	90.8126	222.0561	10.5128	43.6035	91.3616	222.2812	866.20	1719

Table 4: Comparison of exact frequency ratios with approximate estimates for the uniform cantilever beam with zero root offset and zero tip mass;  $\alpha = 0, \mu = 0$ .

Freq. ratio	Method	Rotation speed ratio				Freq. ratio	Method	Rotation speed ratio			
		$\eta_b^z = 0$	$\eta_b^z = 3$	$\eta_b^z = 6$	$\eta_b^z = 12$			$\eta_b^y = 0$	$\eta_b^y = 3$	$\eta_b^y = 6$	$\eta_b^y = 12$
$f_{b1}^z$	Exact [1]	3.5160	4.7973	7.3604	13.1702	$f_{b1}^y$	TITOP beam (1 el.)	3.5160	3.7435	4.2643	5.4640
	TITOP beam (1 el.)	3.5160	4.7974	7.3614	13.1868		TITOP beam (5 el.)	3.5160	3.7434	4.2625	5.4233
	TITOP beam (5 el.)	3.5160	4.7973	7.3604	13.1702		NASTRAN (20 el.)	3.5118	3.7395	4.2595	5.4264
	NASTRAN (20 el.)	3.5118	4.7941	7.3582	13.1699	$f_{b2}^y$	TITOP beam (1 el.)	22.1578	23.2260	26.1815	35.6729
Exact [1]	22.0345	23.3203	26.8091	37.6031	TITOP beam (5 el.)		22.0345	23.1263	26.1284	35.6338	
TITOP beam (1 el.)	22.1578	23.4189	26.8602	37.6372	NASTRAN (20 el.)		21.9402	23.0296	26.0246	35.5066	
$f_{b2}^z$	TITOP beam (5 el.)	22.0345	23.3203	26.8091	37.6031	$f_{b3}^y$	TITOP beam (1 el.)	63.3466	64.4727	67.7383	79.4582
	NASTRAN (20 el.)	21.9402	23.2242	26.7073	37.4796		TITOP beam (5 el.)	61.6973	62.9134	66.4130	78.7026
	Exact [1]	61.6972	62.9850	66.6840	79.6145		NASTRAN (20 el.)	61.2502	62.4602	65.9411	78.1579
	TITOP beam (1 el.)	63.3466	64.5425	68.0035	80.3593						
$f_{b3}^z$	TITOP beam (5 el.)	61.6973	62.9850	66.6840	79.6146						
	NASTRAN (20 el.)	61.2502	62.5322	66.2135	79.0738						

vary linearly [1]. The exact solutions were not found anywhere in the literature for the in-plane dynamics, but this table also provides a comparison of the results with the outputs of a finite element program, NASTRAN. As can be seen from Table 4, the TITOP approach is extremely accurate even at relatively large rotation rates and does not appear to suffer a significant decrease in accuracy for the higher modes, as long as enough beam elements in series are considered. Indeed, the TITOP method has the versatility of finite elements and can be made to converge to the exact solution by increasing the number of elements, as is the case with the conventional finite element method. The NASTRAN results, which can provide very reasonable estimates for many applications, were obtained using 20 beam elements (CBEAM). Furthermore, an Implicit Nonlinear analysis was carried out (SOL 400). The comparison displayed in Table 4, which is conducted for a uniform cantilever beam with rotation speed ratios of  $\eta_b^* = 0, 3, 6, 12$ , also reveals that the calculations presented in this paper closely match the Exact/NASTRAN computations for the first two frequency ratios, even when considering only a single TITOP beam element. It is also evident from the data in Table 4 that, as the rotation speed ratios increase, the frequency ratios rise, due to the centrifugal stiffening effect. Nevertheless, it is worth noting that the in-plane frequency ratios exhibit a slower growth rate compared to the out-of-plane frequency ratios. This phenomenon occurs because the in-plane dynamics also encompass a centrifugal softening effect, which results in a reduction in the natural frequencies as the speed increases.

Let us now consider the system displayed in Fig. 7, composed of a beam and a tip mass, where the beam and tip mass parameters displayed in Table 5 are used to define the system. Furthermore,  $\bar{\mathbf{x}}_p^A = [r, 0, 0]^T$ , with  $r = 2$  m,  $\bar{\boldsymbol{\Theta}}_p^A = \mathbf{0}_{3 \times 1}$ ,  $\bar{\boldsymbol{\omega}}_p^A = [0, 0, \Omega]^T$  and  $m = m^S = 5$  kg. Fig. 8 displays two Campbell diagrams regarding this model, where

$\omega_{b\bullet}^z$  and  $\omega_{b\bullet}^y$  represent the out-of-plane and in-plane natural frequencies, respectively. These plots depict how the first and second natural frequencies for both the in-plane and out-of-plane dynamics change as the angular velocity  $\Omega$  increases. Once more, the influence of the centrifugal stiffening effect is clearly visible. Additionally, it is also noteworthy that, as the number of TITOP beam elements used to model the system is increased, the natural frequencies converge to the results obtained from NASTRAN, since the red and dashed blue lines overlap.

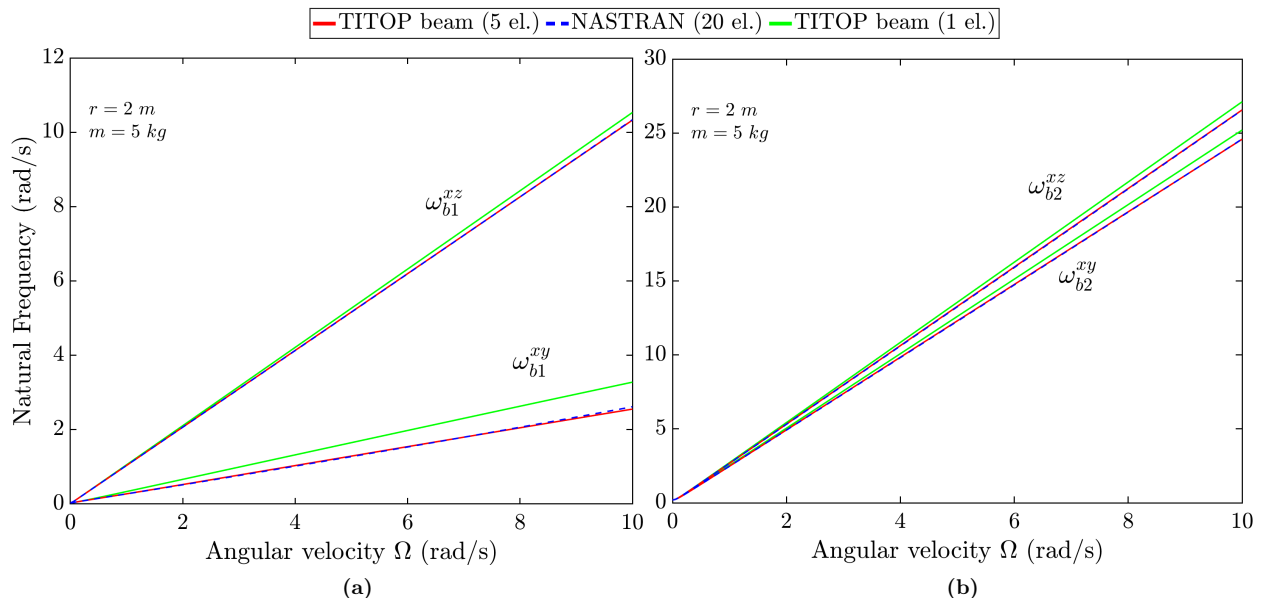


Figure 8: Campbell diagrams for a system composed of a flexible beam and a tip mass: (a) evolution of the first in-plane and out-of-plane natural frequencies  $\omega_{b1}^*$  with respect to  $\Omega$ . (b) evolution of the second in-plane and out-of-plane natural frequencies  $\omega_{b2}^*$  with respect to  $\Omega$ .

## 6. Case study: Spinning and flexible spacecraft

In-situ plasma measurements are used as a crucial tool for examining the characteristics of plasma in space. In order to conduct such measurements, spinning spacecraft platforms are commonly employed due to their numerous advantages. A primary benefit of utilizing a spinning spacecraft is the ability to achieve more consistent sampling of the plasma surroundings. By spinning, the spacecraft allows plasma instruments to capture plasma properties in all directions, thereby obtaining a more comprehensive understanding of the plasma environment [4]. Another advantage of employing a spinning spacecraft platform is its capacity to mitigate spacecraft charging effects. When a spacecraft remains stationary, it can accumulate a negative charge caused by electron buildup on its surface. This charge can disrupt in-situ plasma measurements by causing the spacecraft to repel the plasma. However, when a spacecraft spins, the charge is distributed more evenly across its surface, ultimately reducing the overall charging effect. Furthermore, spinning spacecraft platforms aid in diminishing instrument noise, which can stem from various sources, including electromagnetic interference and thermal fluctuations. By spinning the spacecraft, the noise can be averaged out, resulting in more precise and reliable measurements.

### 6.1. Complete model of the system

For the mission scenario being studied in this paper, a spinning spacecraft is considered, as depicted in Fig. 9. The shape of this spacecraft is inspired by the THOR and Cluster missions. The central cylinder  $\mathcal{B}$  represents the main equipment platform. Two long rod-shaped and flexible booms  $\mathcal{A}_\bullet$  are attached to the rigid hub of the spacecraft  $\mathcal{B}$  and operate when the spacecraft begins to spin. Their function can involve the measurement of fluctuating electrical and magnetic fields in the vicinity of the spacecraft, as demonstrated in the Cluster mission. Alternatively, they may serve as carriers for plasma measurement instruments located at their tips, as exemplified in the THOR project. Within the

scope of this paper, the primary focus is directed towards the second scenario, where the measurement instruments are regarded as tip masses.

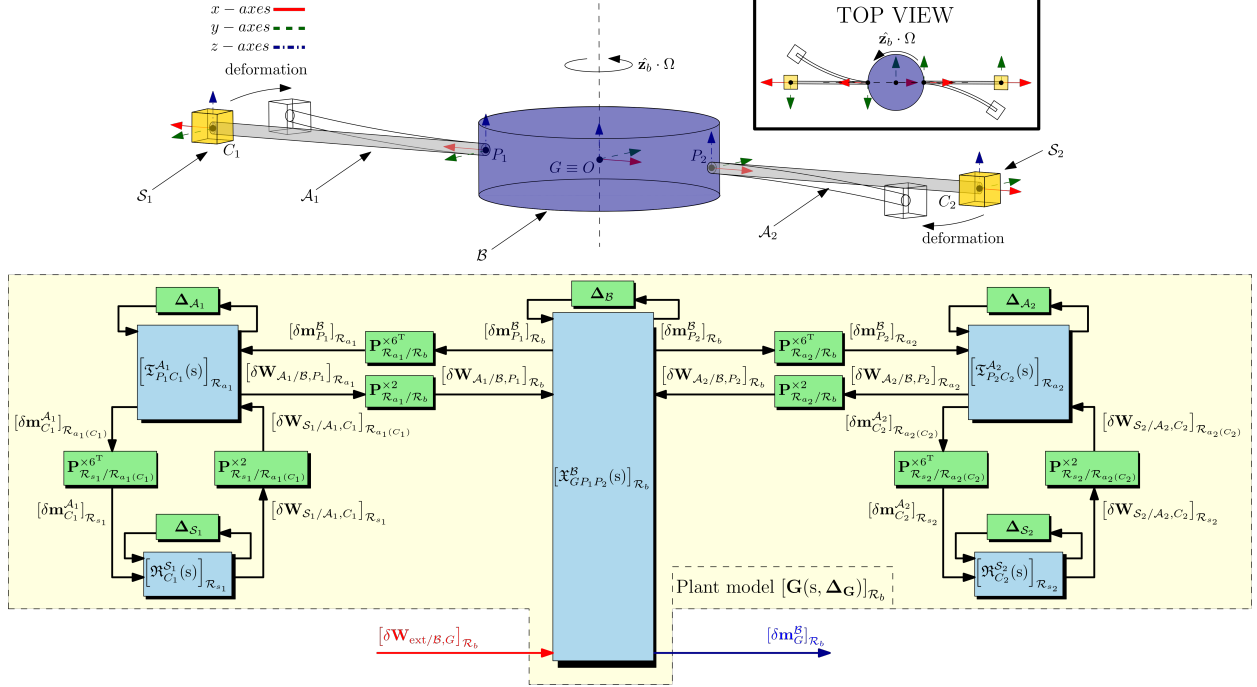


Figure 9: 3D representation and detailed block-diagram representation of a spinning satellite mission scenario composed of one main rigid body, two flexible booms and two tip masses representing two measurement instruments attached to the tip of each boom (Note: for the sake of simplicity, the x-axes are displayed in solid red lines, the y-axes in dashed green lines and the z-axes in dash-dotted blue lines).

A detailed block-diagram representation of the complete system is shown in Fig. 9, where  $\bar{\omega}^* = [0, 0, \Omega]^T$ . Furthermore, the uncertainty block regarding the central rigid hub  $\mathcal{B}$  can be written as  $\Delta_{\mathcal{B}} = \delta_{\Omega} \mathbf{I}_8$ . Following the same logic, the structured uncertainty blocks characterizing the flexible booms and the tip masses are equal to  $\Delta_{\mathcal{A}_i} = \text{diag}(\delta_{\Omega} \mathbf{I}_{169}, \delta_{m_s} \mathbf{I}_{64})$  and  $\Delta_{S_i} = \text{diag}(\delta_{\Omega} \mathbf{I}_4, \delta_{m_s} \mathbf{I}_5)$ , respectively, as explained in section 5. In this case, the number of occurrences of  $\delta_{\Omega}$  and  $\delta_{m_s}$  corresponds to the spinning satellite mission scenario displayed in Fig. 9. For the flexible boom models, the equilibrium conditions are calculated by following the instructions depicted in section 4.

When the full system is assembled, a global LFR representation is obtained, which fully captures the dynamics and interactions between all the subsystems of the scenario being studied. Furthermore, this model also takes into account the various uncertainty effects in a very compact representation. Fig. 9 illustrates the internal structure of the overall LFR model, as well as the interconnections between the several subsystems. In this representation, all the block uncertainties are isolated at the component level.

Since the complete system is spinning, its rotations about the principal axes that correspond to the largest and the smallest moments of inertia are stable. However, the rotation about the axis corresponding to the intermediate principal moment of inertia becomes unstable, leading to unexpected rotations that are the basis of the phenomenon commonly known as the DZHANIBEKOV effect [51]. For this reason, it must be ensured that the rotation about the  $\mathbf{z}_b$ -axis does not correspond to the intermediate principal moment of inertia. Lastly, the presence of symmetry within the system is essential for an equilibrium to be established. All the numerical values and range of variations of the numerous system parameters which are employed in this section are described in Table 5.

## 6.2. Analysis of the spinning and flexible spacecraft dynamics

The Rayleigh damping model is employed to introduce a damping matrix  $\mathbf{D}_{\xi}$  for the flexible booms  $\mathcal{A}_i$  of the spinning spacecraft. This model characterizes damping as a linear combination of the mass and stiffness matrices, facilitating the inclusion of an adaptable damping ratio for the associated modes. Therefore, the method presented in

[54] is used to generate the damping matrix  $\mathbf{D}_\xi = \alpha \mathbf{M}_{ff} + \beta \mathbf{K}_{ff}$ , with  $\alpha = 0.0001 \text{ s}^{-1}$  and  $\beta = 0.0012 \text{ s}$ . Ultimately, the matrix  $\mathbf{D}_{ff}$  is replaced by  $\widehat{\mathbf{D}}_{ff} = \mathbf{D}_{ff} + \mathbf{D}_\xi$  in the state-space representations of the flexible spinning booms (displayed in Eq. (50)), so that the selected damping is taken into account.

Let us now analyze the singular values of the spinning and flexible spacecraft model  $[\mathbf{G}(s, \Delta_{\mathbf{G}})]_{\mathcal{R}_b}$  for different values of  $\Omega$  and  $m^{S_\bullet}$ , where  $\Delta_{\mathbf{G}} = \text{diag}(\Delta_{\mathcal{B}}, \Delta_{\mathcal{A}_1}, \Delta_{\mathcal{A}_2}, \Delta_{\mathcal{S}_1}, \Delta_{\mathcal{S}_2})$ . For instance, if the transfer function from the second component of the external torque  $\delta \mathbf{T}_{\text{ext}/\mathcal{B},G}$  to the second component of the angular acceleration  $\delta \dot{\omega}_G^{\mathcal{B}}$  is considered, Figs. 10 and 11 show how the natural frequencies of the system evolve with respect to  $\Omega$  and  $m^{S_\bullet}$ . The complete system has 52 poles, where 12 poles are associated with the rigid hub model  $[\mathbf{x}_{GP_1P_2}^{\mathcal{B}}(s)]_{\mathcal{R}_b}$  and the other 40 poles are related to the two spinning beam models  $[\mathbf{x}_{P_\bullet C_\bullet}^{\mathcal{A}_\bullet}(s)]_{\mathcal{R}_{a_\bullet}}$ . In Figs. 10 and 11, the number of flexible modes which are visible correspond to the number of observable poles linked with the minimal realization of the system  $[\mathbf{G}(s, \Delta_{\mathbf{G}})]_{\mathcal{R}_b}$  when taking into account the selected channel  $\delta \mathbf{T}_{\text{ext}/\mathcal{B},G}\{2\} \rightarrow \delta \dot{\omega}_G^{\mathcal{B}}\{2\}$ . Since  $[\mathbf{G}(s, \Delta_{\mathbf{G}})]_{\mathcal{R}_b}$  represents the inverse linearized dynamic model of the whole system projected in  $\mathcal{R}_b$  and the channel  $\delta \mathbf{T}_{\text{ext}/\mathcal{B},G}\{2\} \rightarrow \delta \dot{\omega}_G^{\mathcal{B}}\{2\}$  is being analyzed, the static gain of the plot in Fig. 10 where  $\Omega = 0 \text{ rad s}^{-1}$  represents the inverse of the second moment of inertia of the complete spacecraft, measured at the point  $G$  and written in  $\mathcal{R}_b$ .

In Fig. 9, the centrifugal forces applied by the tip masses  $\mathcal{S}_\bullet$  to the spinning beams  $\mathcal{A}_\bullet$  are determined by the equation  $\overline{\mathbf{W}}_{\mathcal{S}_\bullet/\mathcal{A}_\bullet,C_\bullet}\{1\} = m^{S_\bullet} (l^{\mathcal{A}_\bullet} + r) \Omega^2$ . These forces are projected onto the beams' body frames, labeled as  $\mathcal{R}_{a_\bullet}$ . They are also accountable for the centrifugal stiffening effect, which causes the natural frequencies of the system to shift to the right in the singular values plots as the values of  $\Omega$  and  $m^{S_\bullet}$  increase, as displayed in Figs. 10 and 11. Notably, this effect is more pronounced for  $\Omega$ , since it appears squared in the expression for the centrifugal forces.

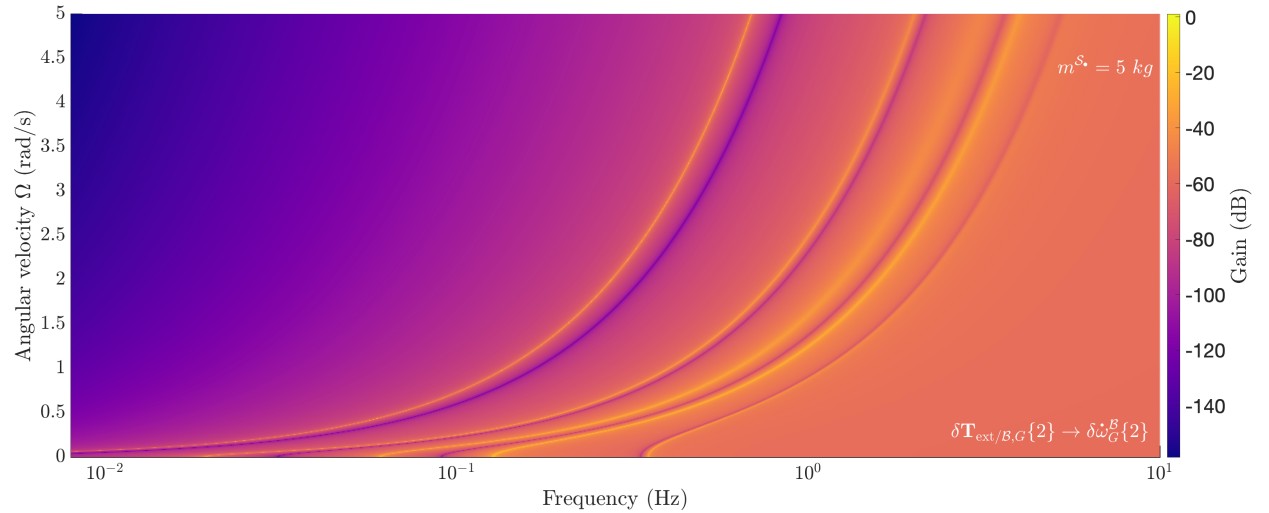


Figure 10: Singular values of the model  $[\mathbf{G}(s, \Delta_{\mathbf{G}})]_{\mathcal{R}_b}$  with respect to the angular velocity  $\Omega$  and along a dense grid of frequencies ( $\delta \mathbf{T}_{\text{ext}/\mathcal{B},G}\{2\} \rightarrow \delta \dot{\omega}_G^{\mathcal{B}}\{2\}$  channel).

## 7. Conclusion

This paper outlined a comprehensive study on the analytical modeling and analysis of a spinning, flexible and uniform Euler-Bernoulli beam, with a specific focus on its application to a spinning spacecraft mission scenario. First and foremost, the presented framework shows how to build a very compact representation of a six degrees of freedom analytical model that fully captures the complex dynamics of a spinning beam, including the bending, traction and torsion effects. This model is represented as a linear fractional representation and is parameterized based on the angular velocity of the beam. Such a model is instrumental for robust control system design in spacecraft applications, where precise control of the flexible structures is critical. Moreover, the TITOP beam model was validated by comparing the natural frequencies with results from a traditional finite element code, ensuring the accuracy and

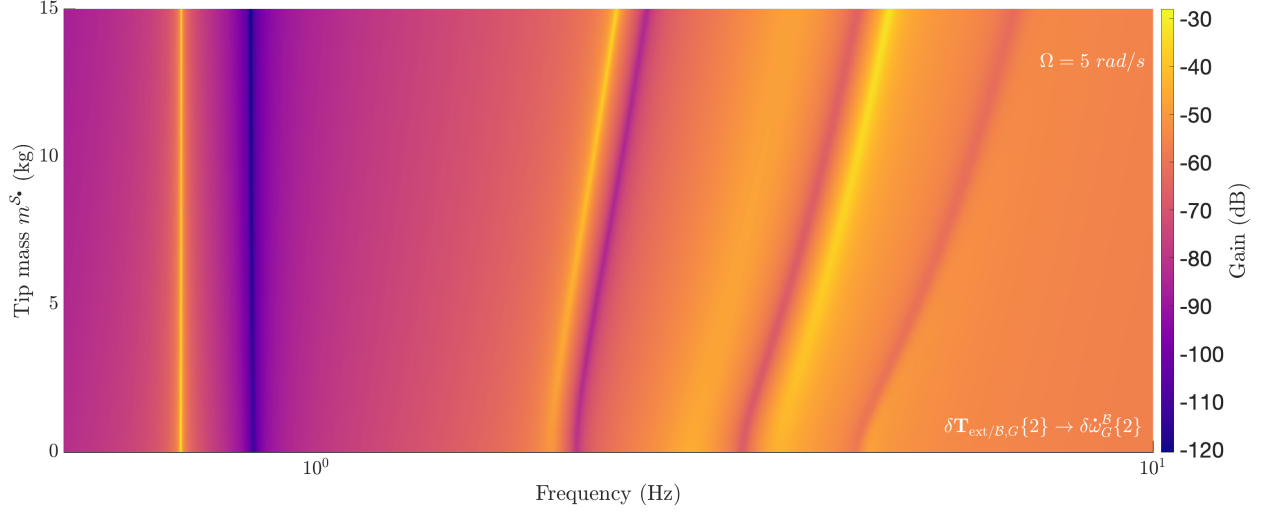


Figure 11: Singular values of the model  $[G(s, \Delta_G)]_{R_b}$  for different tip mass values  $m^{S_*}$  and along a dense grid of frequencies ( $\delta T_{\text{ext}/B,G}\{2\} \rightarrow \delta \dot{\omega}_G^B\{2\}$  channel).

reliability of this analytical approach. The paper also provides a valuable insight into the dynamics of a spinning spacecraft mission, which includes a central body, two flexible booms and two tip masses. This multibody modeling and analysis offers a practical understanding of the behavior of such systems under spinning conditions, which can be beneficial for the design and operation of similar missions, like THOR and Cluster.

Table 5: Spinning spacecraft mechanical data and equilibrium conditions.

Parameter	Description	Value	
$\overline{GP}$	distance vector between $G$ and $P_*$ in equilibrium and written in $R_b$	$[\pm 2, 0, 0]$ m	
$m^B$	mass of $B$	500 kg	
Central rigid body $B$	$\begin{bmatrix} J_{xx}^B & J_{xy}^B & J_{xz}^B \\ J_{xy}^B & J_{yy}^B & J_{yz}^B \\ J_{xz}^B & J_{yz}^B & J_{zz}^B \end{bmatrix}$	$\begin{bmatrix} 570.42 & 0 & 0 \\ & 570.42 & 0 \\ & & 1000 \end{bmatrix}$ kg m <sup>2</sup>	
$\mathcal{T}_{R_{a_1}/R_b}$	change of frame DCM between $R_{a_1}$ and $R_b$	$\begin{bmatrix} -1 & 0 & 0 \\ 0 & -1 & 0 \\ 0 & 0 & 1 \end{bmatrix}$	
$\mathcal{T}_{R_{a_2}/R_b}$	change of frame DCM between $R_{a_2}$ and $R_b$	$I_3$	
$\overline{V}_G^B$	inertial velocity vector of the body $B$ computed at the point $G$ in equilibrium	$\mathbf{0}_{3 \times 1}$ m s <sup>-1</sup>	
$\overline{\omega}_G^B$	angular velocity vector of the body $B$ computed at the point $G$ in equilibrium	$[0, 0, \Omega]^T$ rad s <sup>-1</sup>	
$l^A$	length of $A_*$	50 m	
$\rho^A$	mass density of $A_*$	2700 kg m <sup>-3</sup>	
$S^A$	cross-sectional area of $A_*$	$3.14 \times 10^{-4}$ m <sup>2</sup>	
$E^A$	Young's modulus of $A_*$	$7 \times 10^{10}$ N m <sup>-2</sup>	
$\nu^A$	Poisson's ratio of $A_*$	0.33	
$J_{px}^A$	second polar moment of area of $A_*$ with respect to the $x_a$ -axis	$1.57 \times 10^{-8}$ m <sup>4</sup>	
$J_{ya}^A$	second moment of area of $A_*$ with respect to the $y_a$ -axis	$7.85 \times 10^{-9}$ m <sup>4</sup>	
$J_{za}^A$	second moment of area of $A_*$ with respect to the $z_a$ -axis	$7.85 \times 10^{-9}$ m <sup>4</sup>	
Flexible booms $A_*$	$\mathcal{T}_{R_{a_1}/R_{a_2}(C_*)}$	$I_3$	
	$\overline{x}_{P_*}^A$	distance vector between $O$ and $P_*$ in equilibrium and written in $R_{a_*}$	$[r = 2, 0, 0]^T$ m
	$\Theta_{P_*}^A$	Euler angles of the beam $A_*$ computed at the point $P_*$ in equilibrium	$\mathbf{0}_{3 \times 1}$ rad
	$\overline{v}_{P_*}^A$	inertial velocity vector of the beam $A_*$ computed at the point $P_*$ in equilibrium	$[0, r\Omega, 0]^T$ m s <sup>-1</sup>
	$\overline{\omega}_{P_*}^A$	angular velocity vector of the beam $A_*$ computed at the point $P_*$ in equilibrium	$[0, 0, \Omega]^T$ rad s <sup>-1</sup>
	$\overline{W}_{S_*/A_*,C_*}$	wrench vector applied by the body $S_*$ to the body $A_*$ at the point $C_*$ in equilibrium	$[m^{S_*} (l^{A_*} + r)\Omega^2, 0, 0, 0, 0, 0]^T$ [N N m]
Tip masses $S_*$	$\begin{bmatrix} J_{xx}^{S_*} & J_{xy}^{S_*} & J_{xz}^{S_*} \\ J_{xy}^{S_*} & J_{yy}^{S_*} & J_{yz}^{S_*} \\ J_{xz}^{S_*} & J_{yz}^{S_*} & J_{zz}^{S_*} \end{bmatrix}$	$\begin{bmatrix} 0 & 0 & 0 \\ 0 & 0 & 0 \\ 0 & 0 & 0 \end{bmatrix}$ kg m <sup>2</sup>	
	$\overline{v}_{C_*}^{S_*}$	inertial velocity vector of the beam $S_*$ computed at the point $C_*$ in equilibrium	$[0, (l^{A_*} + r)\Omega, 0]^T$ m s <sup>-1</sup>
	$\overline{\omega}_{C_*}^{S_*}$	angular velocity vector of the body $S_*$ computed at the point $C_*$ in equilibrium	$[0, 0, \Omega]^T$ rad s <sup>-1</sup>

## Appendix A. Choice of the modal decomposition

A decomposition based on fifth-order polynomial shape functions [43, 49] is selected to build the TITOP model  $\left[\mathfrak{I}_{PC}^{\mathcal{A}}(s)\right]_{\mathcal{R}_a}$ . In this approach, the deflection  $\tilde{v}(x, t)$  in the moving frame  $\mathcal{R}_a$  is expressed as:

$$\tilde{v}(x, t) = a_2^y(t)x^2 + a_3^y(t)x^3 + a_4^y(t)x^4 + a_5^y(t)x^5 \quad (\text{A.1})$$

This fifth-order polynomial ensures that  $\tilde{v}(0, t) = \frac{\partial \tilde{v}}{\partial x}(0, t) = 0, \forall t$ . The coefficients  $a_i^y(t)$  are then expressed as a function of four time-domain functions  $q_i^y(t)$  defined by:

$$\mathbf{q}_y(t) = \left[ \frac{\partial^2 \tilde{v}}{\partial x^2}(0, t) \quad \tilde{v}(l^{\mathcal{A}}, t) \quad \frac{\partial \tilde{v}}{\partial x}(l^{\mathcal{A}}, t) \quad \frac{\partial^2 \tilde{v}}{\partial x^2}(l^{\mathcal{A}}, t) \right]^T \quad (\text{A.2})$$

The shape functions vector reads:

$$\Phi_y(x) = \begin{bmatrix} \frac{1}{2}x^2 - \frac{3}{2l^{\mathcal{A}}}x^3 + \frac{3}{2l^{\mathcal{A}^2}}x^4 - \frac{1}{2l^{\mathcal{A}^3}}x^5 \\ \frac{10}{l^{\mathcal{A}^3}}x^3 - \frac{15}{l^{\mathcal{A}^4}}x^4 + \frac{6}{l^{\mathcal{A}^5}}x^5 \\ \frac{-4}{l^{\mathcal{A}^2}}x^3 + \frac{7}{l^{\mathcal{A}^3}}x^4 - \frac{3}{l^{\mathcal{A}^4}}x^5 \\ \frac{1}{2l^{\mathcal{A}}}x^3 - \frac{1}{l^{\mathcal{A}^2}}x^4 + \frac{1}{2l^{\mathcal{A}^3}}x^5 \end{bmatrix} \quad (\text{A.3})$$

A similar process is achieved for the deflection  $\tilde{w}(x, t)$  in the moving frame  $\mathcal{R}_a$ , with:

$$\mathbf{q}_z(t) = \left[ \frac{\partial^2 \tilde{w}}{\partial x^2}(0, t) \quad \tilde{w}(l^{\mathcal{A}}, t) \quad \frac{\partial \tilde{w}}{\partial x}(l^{\mathcal{A}}, t) \quad \frac{\partial^2 \tilde{w}}{\partial x^2}(l^{\mathcal{A}}, t) \right]^T \quad \text{and} \quad \Phi_z(x) = \Phi_y(x) \quad (\text{A.4})$$

## Appendix B. Matrices used to model the state-space representation of the spinning beam

$$\begin{aligned} \mathbf{M}_p &= \rho^{\mathcal{A}} S^{\mathcal{A}} \int_0^{l^{\mathcal{A}}} (*\mathbf{P}_0(x)) dx & \mathbf{M}_{\sigma\sigma} &= \rho^{\mathcal{A}} S^{\mathcal{A}} \int_0^{l^{\mathcal{A}}} \sigma(x)\sigma(x) dx \\ \mathbf{M}_m &= \rho^{\mathcal{A}} S^{\mathcal{A}} \int_0^{l^{\mathcal{A}}} \mathbf{M}_1(x) dx & \mathbf{M}_{\sigma} &= \rho^{\mathcal{A}} S^{\mathcal{A}} \int_0^{l^{\mathcal{A}}} \sigma(x) dx \\ \mathbf{K}_{soft} &= \rho^{\mathcal{A}} S^{\mathcal{A}} \int_0^{l^{\mathcal{A}}} -\mathbf{M}_1(x)(*\overline{\omega}_p^{\mathcal{A}})^2 \mathbf{M}_1^T(x) dx & \mathbf{D}_{soft} &= \rho^{\mathcal{A}} S^{\mathcal{A}} \int_0^{l^{\mathcal{A}}} \mathbf{M}_1(x)(*\overline{\omega}_p^{\mathcal{A}}) \mathbf{M}_1^T(x) dx \\ \mathbf{M}_{mpw} &= \rho^{\mathcal{A}} S^{\mathcal{A}} \int_0^{l^{\mathcal{A}}} \mathbf{M}_1(x)(*\overline{\omega}_p^{\mathcal{A}})(*\mathbf{P}_0(x)) dx & \mathbf{E}_i &= \rho^{\mathcal{A}} S^{\mathcal{A}} \int_0^{l^{\mathcal{A}}} \begin{bmatrix} \mathbf{E}^{yz}(x) & \mathbf{0}_{2N \times 2} \\ \mathbf{0}_{2 \times 2N} & \mathbf{0}_{2 \times 2} \end{bmatrix} dx \\ \mathbf{E}_{ix} &= \rho^{\mathcal{A}} S^{\mathcal{A}} \int_0^{l^{\mathcal{A}}} \begin{bmatrix} x \mathbf{E}^{yz}(x) & \mathbf{0}_{2N \times 2} \\ \mathbf{0}_{2 \times 2N} & \mathbf{0}_{2 \times 2} \end{bmatrix} dx & \mathbf{E}_l &= \begin{bmatrix} \mathbf{E}^{yz}(l^{\mathcal{A}}) & \mathbf{0}_{2N \times 2} \\ \mathbf{0}_{2 \times 2N} & \mathbf{0}_{2 \times 2} \end{bmatrix} \end{aligned} \quad (\text{B.1})$$

$$\mathbf{P}_{\sigma 1} = \begin{bmatrix} m^{\mathcal{A}} \frac{J_{px}^{\mathcal{A}}}{S^{\mathcal{A}}} & 0 & 0 \\ 0 & 0 & 0 \\ 0 & 0 & 0 \end{bmatrix} \quad \mathbf{P}_{\sigma 2} = \begin{bmatrix} \mathbf{0}_{N \times 1} & \mathbf{0}_{N \times 1} & \mathbf{0}_{N \times 1} \\ \mathbf{0}_{N \times 1} & \mathbf{0}_{N \times 1} & \mathbf{0}_{N \times 1} \\ 0 & 0 & 0 \\ \frac{J_{px}^{\mathcal{A}}}{S^{\mathcal{A}}} \mathbf{M}_{\sigma} & 0 & 0 \end{bmatrix} \quad \mathbf{P}_{\sigma 3} = \begin{bmatrix} \mathbf{0}_{N \times N} & \mathbf{0}_{N \times N} & \mathbf{0}_{N \times 1} & \mathbf{0}_{N \times 1} \\ \mathbf{0}_{N \times N} & \mathbf{0}_{N \times N} & \mathbf{0}_{N \times 1} & \mathbf{0}_{N \times 1} \\ \mathbf{0}_{1 \times N} & \mathbf{0}_{1 \times N} & 0 & 0 \\ \mathbf{0}_{1 \times N} & \mathbf{0}_{1 \times N} & 0 & \frac{J_{px}^{\mathcal{A}}}{S^{\mathcal{A}}} \mathbf{M}_{\sigma\sigma} \end{bmatrix} \quad (\text{B.2})$$

$$\begin{aligned} \mathbf{J}_p &= \rho^{\mathcal{A}} S^{\mathcal{A}} \int_0^{l^{\mathcal{A}}} -(*\mathbf{P}_0(x))^2 dx + \mathbf{P}_{\sigma 1} & \mathbf{M}_{mp} &= \rho^{\mathcal{A}} S^{\mathcal{A}} \int_0^{l^{\mathcal{A}}} \mathbf{M}_1(x)(*\mathbf{P}_0(x))^T dx + \mathbf{P}_{\sigma 2} \\ \mathbf{M}_{mm} &= \rho^{\mathcal{A}} S^{\mathcal{A}} \int_0^{l^{\mathcal{A}}} \mathbf{M}_1(x) \mathbf{M}_1^T(x) dx + \mathbf{P}_{\sigma 3} \end{aligned} \quad (\text{B.3})$$

$$\mathbf{M}_{\mathcal{T}} = \begin{bmatrix} m^{\mathcal{A}} \mathbf{I}_3 & \mathbf{M}_p^T & \mathbf{M}_m^T \\ \mathbf{M}_p & \mathbf{J}_p & \mathbf{M}_{mp}^T \\ \mathbf{M}_m & \mathbf{M}_{mp} & \mathbf{M}_{mm} \end{bmatrix} \quad (\text{B.4})$$

$$\mathbf{K}_{\mathcal{T}} = \begin{bmatrix} \mathbf{0}_{3 \times 3} & \mathbf{0}_{3 \times 3} & \mathbf{0}_{3 \times (2N+2)} \\ \mathbf{0}_{3 \times 3} & \mathbf{0}_{3 \times 3} & \mathbf{0}_{3 \times (2N+2)} \\ \mathbf{0}_{(2N+2) \times 3} & \mathbf{0}_{(2N+2) \times 3} & \mathbf{K}_{soft} + (\bar{\omega}_p^{\mathcal{A}}\{2\}\bar{\mathbf{v}}_p^{\mathcal{A}}\{3\} - \bar{\omega}_p^{\mathcal{A}}\{3\}\bar{\mathbf{v}}_p^{\mathcal{A}}\{2\})\mathbf{E}_i - ((\bar{\omega}_p^{\mathcal{A}}\{3\})^2 + (\bar{\omega}_p^{\mathcal{A}}\{2\})^2)\mathbf{E}_{ix} \end{bmatrix} \quad (\text{B.5})$$

$$\mathbf{G}_{\mathcal{T}} = \begin{bmatrix} \mathbf{0}_{3 \times 3} & \mathbf{0}_{3 \times 3} & \mathbf{0}_{3 \times (2N+2)} \\ \mathbf{0}_{3 \times 3} & \mathbf{0}_{3 \times 3} & \mathbf{0}_{3 \times (2N+2)} \\ -2\mathbf{M}_m(*\bar{\omega}_p^{\mathcal{A}}) & 2\mathbf{M}_m(*\bar{\mathbf{v}}_p^{\mathcal{A}}) + 2\mathbf{M}_{mp}(*\bar{\omega}_p^{\mathcal{A}}) + 4\mathbf{M}_{mp\omega} & -2\bar{\mathbf{v}}_p^{\mathcal{A}}\{1\}\mathbf{E}_i - 2\mathbf{D}_{soft} \end{bmatrix} \quad (\text{B.6})$$

$$\mathbf{C}_Q^T = \begin{bmatrix} \mathbf{0}_{1 \times 3} & \mathbf{0}_{1 \times 3} & \bar{\mathbf{v}}_p^{\mathcal{A}T}(*\bar{\omega}_p^{\mathcal{A}})\mathbf{M}_m^T + (*\bar{\omega}_p^{\mathcal{A}})^T\mathbf{M}_{mp\omega}^T \end{bmatrix} \quad \mathbf{C}_{\dot{Q}}^T = \begin{bmatrix} \bar{\mathbf{v}}_p^{\mathcal{A}} \\ *\bar{\omega}_p^{\mathcal{A}} \end{bmatrix}^T \mathbf{M}_{\mathcal{T}(1:6,:)} \quad (\text{B.7})$$

$$\begin{bmatrix} (*\bar{\omega}_p^{\mathcal{A}}) & \mathbf{0}_{3 \times 3} \\ (*\bar{\mathbf{v}}_p^{\mathcal{A}}) & (*\bar{\omega}_p^{\mathcal{A}}) \end{bmatrix} \frac{\partial \mathcal{L}}{\partial \begin{bmatrix} \delta \bar{\mathbf{v}}_p^{\mathcal{A}} \\ \delta \bar{\omega}_p^{\mathcal{A}} \end{bmatrix}} = \mathbf{M}_{\mathcal{L}}\delta \mathbf{Q}_v(t) + \mathbf{J}_{\mathcal{L}}\delta \mathbf{Q}_p(t) + \mathbf{C}_{\mathcal{L}} \quad (\text{B.8})$$

$$\mathbf{M}_{\mathcal{L}} = \begin{bmatrix} (*\bar{\omega}_p^{\mathcal{A}}) & \mathbf{0}_{3 \times 3} \\ (*\bar{\mathbf{v}}_p^{\mathcal{A}}) & (*\bar{\omega}_p^{\mathcal{A}}) \end{bmatrix} \mathbf{M}_{\mathcal{T}(1:6,:)} - \begin{bmatrix} \mathbf{0}_{3 \times 3} & m^{\mathcal{A}}(*\bar{\mathbf{v}}_p^{\mathcal{A}}) + (*\mathbf{M}_p^T\bar{\omega}_p^{\mathcal{A}}) & \mathbf{0}_{3 \times (2N+2)} \\ m^{\mathcal{A}}(*\bar{\mathbf{v}}_p^{\mathcal{A}}) + (*\mathbf{M}_p^T\bar{\omega}_p^{\mathcal{A}}) & (*\mathbf{M}_p\bar{\mathbf{v}}_p^{\mathcal{A}}) + (*\mathbf{J}_p\bar{\omega}_p^{\mathcal{A}}) & \mathbf{0}_{3 \times (2N+2)} \end{bmatrix} \quad (\text{B.9})$$

$$\mathbf{J}_{\mathcal{L}} = \begin{bmatrix} (*\bar{\omega}_p^{\mathcal{A}}) & \mathbf{0}_{3 \times 3} \\ (*\bar{\mathbf{v}}_p^{\mathcal{A}}) & (*\bar{\omega}_p^{\mathcal{A}}) \end{bmatrix} \frac{1}{2}(\mathbf{G}_{\mathcal{T}(1:6,:)}^T) \quad \mathbf{C}_{\mathcal{L}} = \begin{bmatrix} (*\bar{\omega}_p^{\mathcal{A}}) & \mathbf{0}_{3 \times 3} \\ (*\bar{\mathbf{v}}_p^{\mathcal{A}}) & (*\bar{\omega}_p^{\mathcal{A}}) \end{bmatrix} \mathbf{C}_{\dot{Q}(1:6,1)} \quad (\text{B.10})$$

$$\bar{\boldsymbol{\tau}}_{CP} = \begin{bmatrix} \mathbf{I}_3 & \begin{bmatrix} 0 & 0 & 0 \\ 0 & 0 & l^{\mathcal{A}} \\ 0 & -l^{\mathcal{A}} & 0 \end{bmatrix} \\ \mathbf{0}_{3 \times 3} & \mathbf{I}_3 \end{bmatrix} \quad \mathbf{G}_{vv} = \begin{bmatrix} \mathbf{M}_1^T(l^{\mathcal{A}}) \\ \mathbf{M}_2^T(l^{\mathcal{A}}) \end{bmatrix} \quad (\text{B.11})$$

$$\mathbf{M}_3^T = \begin{bmatrix} \Phi_y^T(l^{\mathcal{A}})(\bar{\mathbf{v}}_p^{\mathcal{A}}\{2\} + l^{\mathcal{A}}\bar{\omega}_p^{\mathcal{A}}\{3\}) & \Phi_z^T(l^{\mathcal{A}})(\bar{\mathbf{v}}_p^{\mathcal{A}}\{3\} - l^{\mathcal{A}}\bar{\omega}_p^{\mathcal{A}}\{2\}) & 0 & 0 \\ -\Phi_y^T(l^{\mathcal{A}})\bar{\mathbf{v}}_p^{\mathcal{A}}\{1\} & \mathbf{0}_{1 \times N} & 0 & \sigma(l^{\mathcal{A}})(\bar{\mathbf{v}}_p^{\mathcal{A}}\{3\} - l^{\mathcal{A}}\bar{\omega}_p^{\mathcal{A}}\{2\}) \\ \mathbf{0}_{1 \times N} & -\Phi_z^T(l^{\mathcal{A}})\bar{\mathbf{v}}_p^{\mathcal{A}}\{1\} & 0 & -\sigma(l^{\mathcal{A}})(\bar{\mathbf{v}}_p^{\mathcal{A}}\{2\} + l^{\mathcal{A}}\bar{\omega}_p^{\mathcal{A}}\{3\}) \end{bmatrix} \quad (\text{B.12})$$

$$\mathbf{G}_{vp} = \begin{bmatrix} (*\bar{\omega}_p^{\mathcal{A}})\mathbf{M}_1^T(l^{\mathcal{A}}) + \mathbf{M}_3^T \\ \begin{bmatrix} \Phi_y^T(l^{\mathcal{A}})\bar{\omega}_p^{\mathcal{A}}\{2\} & \Phi_z^T(l^{\mathcal{A}})\bar{\omega}_p^{\mathcal{A}}\{3\} & 0 & 0 \\ -\Phi_y^T(l^{\mathcal{A}})\bar{\omega}_p^{\mathcal{A}}\{1\} & \mathbf{0}_{1 \times N} & 0 & \sigma(l^{\mathcal{A}})\bar{\omega}_p^{\mathcal{A}}\{3\} \\ \mathbf{0}_{1 \times N} & -\Phi_z^T(l^{\mathcal{A}})\bar{\omega}_p^{\mathcal{A}}\{1\} & 0 & -\sigma(l^{\mathcal{A}})\bar{\omega}_p^{\mathcal{A}}\{2\} \end{bmatrix} \end{bmatrix} \quad (\text{B.13})$$

$$\mathbf{G}_p = \begin{bmatrix} \begin{bmatrix} \Phi_y^T(l^{\mathcal{A}})\bar{\mathbf{x}}_p^{\mathcal{A}}\{2\} & \Phi_z^T(l^{\mathcal{A}})\bar{\mathbf{x}}_p^{\mathcal{A}}\{3\} & \tau(l^{\mathcal{A}}) & 0 \\ -\Phi_y^T(l^{\mathcal{A}})(\bar{\mathbf{x}}_p^{\mathcal{A}}\{1\} + l^{\mathcal{A}}) + \Phi_y^T(l^{\mathcal{A}}) & \mathbf{0}_{1 \times N} & 0 & \sigma(l^{\mathcal{A}})\bar{\mathbf{x}}_p^{\mathcal{A}}\{3\} \\ \mathbf{0}_{1 \times N} & -\Phi_z^T(l^{\mathcal{A}})(\bar{\mathbf{x}}_p^{\mathcal{A}}\{1\} + l^{\mathcal{A}}) + \Phi_z^T(l^{\mathcal{A}}) & 0 & -\sigma(l^{\mathcal{A}})\bar{\mathbf{x}}_p^{\mathcal{A}}\{2\} \end{bmatrix} \\ \mathbf{M}_2^T(l) \end{bmatrix} \quad (\text{B.14})$$

$$\mathbf{M}_l = \begin{bmatrix} \bar{\boldsymbol{\tau}}_{CP} \\ \mathbf{0}_{6 \times 6} \\ \mathbf{0}_{6 \times 6} \end{bmatrix} \quad \mathbf{D}_l = \begin{bmatrix} \mathbf{0}_{6 \times 6} \\ \bar{\boldsymbol{\tau}}_{CP} \\ \mathbf{0}_{6 \times 6} \end{bmatrix} \quad \mathbf{K}_l = \begin{bmatrix} \mathbf{0}_{6 \times 6} \\ \mathbf{0}_{6 \times 6} \\ \mathbf{I}_6 \end{bmatrix} \quad \mathbf{M}_r = \begin{bmatrix} \mathbf{G}_{vv} \\ \mathbf{0}_{6 \times 10} \\ \mathbf{0}_{6 \times 10} \end{bmatrix} \quad \mathbf{D}_r = \begin{bmatrix} \mathbf{G}_{vp} \\ \mathbf{G}_{vv} \\ \mathbf{0}_{6 \times 10} \end{bmatrix} \quad \mathbf{K}_r = \begin{bmatrix} \mathbf{0}_{6 \times 10} \\ \mathbf{G}_{vp} \\ \mathbf{G}_p \end{bmatrix} \quad (\text{B.15})$$

$$\bar{\mathbf{N}} = \begin{bmatrix} -\mathbf{I}_6 & \bar{\boldsymbol{\tau}}_{CP}^T \\ \mathbf{0}_{(2N+2) \times 6} & \begin{bmatrix} \mathbf{M}_1(l^{\mathcal{A}}) & \mathbf{M}_2(l^{\mathcal{A}}) \end{bmatrix} \end{bmatrix} \quad (\text{B.16})$$

$$\mathbf{K}_c = - \begin{bmatrix} \boldsymbol{\Phi}_y^T(l^{\mathcal{A}}) \bar{\mathbf{W}}_{\bullet/\mathcal{A},C}\{3\} & -\boldsymbol{\Phi}_z^T(l^{\mathcal{A}}) \bar{\mathbf{W}}_{\bullet/\mathcal{A},C}\{2\} & 0 & 0 \\ \mathbf{0}_{1 \times N} & \boldsymbol{\Phi}_z^T(l^{\mathcal{A}}) \bar{\mathbf{W}}_{\bullet/\mathcal{A},C}\{1\} & -\tau(l^{\mathcal{A}}) \bar{\mathbf{W}}_{\bullet/\mathcal{A},C}\{3\} & 0 \\ -\boldsymbol{\Phi}_y^T(l^{\mathcal{A}}) \bar{\mathbf{W}}_{\bullet/\mathcal{A},C}\{1\} & \mathbf{0}_{1 \times N} & \tau(l^{\mathcal{A}}) \bar{\mathbf{W}}_{\bullet/\mathcal{A},C}\{2\} & 0 \end{bmatrix} \quad (\text{B.17})$$

$$\mathbf{F}_c = \begin{bmatrix} \mathbf{0}_{3 \times 3} & \mathbf{0}_{3 \times 3} & \mathbf{0}_{3 \times (2N+2)} \\ \mathbf{0}_{3 \times 3} & \mathbf{0}_{3 \times 3} & \mathbf{K}_c \\ \mathbf{0}_{(2N+2) \times 3} & \mathbf{0}_{(2N+2) \times 3} & \mathbf{E}_l \bar{\mathbf{W}}_{\bullet/\mathcal{A},C}\{1\} \end{bmatrix} + \begin{bmatrix} \mathbf{0}_{(6+2N+2) \times 6} & \bar{\mathbf{N}}_{(:,7:12)} \mathbf{W}_C \end{bmatrix} \quad (\text{B.18})$$

## Funding Sources

This work was funded by ISAE-SUPAERO.

## References

- [1] A. D. Wright, C. E. Smith, R. W. Thresher, J. L. C. Wang, Vibration Modes of Centrifugally Stiffened Beams, *Journal of Applied Mechanics* 49 (1982) 197–202.
- [2] L. Puig, A. Barton, N. Rando, A review on large deployable structures for astrophysics missions, *Acta Astronautica* 67 (2010) 12–26.
- [3] C. P. Escoubet, M. Fehringer, M. Goldstein, The cluster mission, *Annales Geophysicae* 19 (2001) 1197–1200.
- [4] A. Vaivads, A. Retinò, J. Soucek, Y. V. Khotyaintsev, F. Valentini, C. P. Escoubet, O. Alexandrova, M. André, S. D. Bale, M. Balikhin, et al., Turbulence heating observer – satellite mission proposal, *Journal of Plasma Physics* 82 (2016) 905820501.
- [5] A. A. Shabana, Flexible multibody dynamics: Review of past and recent developments, *Multibody System Dynamics* 1 (1997) 189–222.
- [6] N. Auciello, M. Maurizi, On the natural vibrations of tapered beams with attached inertia elements, *Journal of Sound and Vibration* 199 (1997) 522–530.
- [7] D. Zhou, Y. Cheung, The free vibration of a type of tapered beams, *Computer Methods in Applied Mechanics and Engineering* 188 (2000) 203–216.
- [8] I. Elishakoff, R. Becquet, Closed-form solutions for natural frequency for inhomogeneous beams with one sliding support and the other pinned, *Journal of Sound and Vibration* 238 (2000) 529–539.
- [9] Y. Khan, Q. Wu, Homotopy perturbation transform method for nonlinear equations using he’s polynomials, *Computers & Mathematics with Applications* 61 (2011) 1963–1967. *Advances in Nonlinear Dynamics*.
- [10] Y. Khan, H. Vázquez-Leal, N. Faraz, An auxiliary parameter method using adomian polynomials and laplace transformation for nonlinear differential equations, *Applied Mathematical Modelling* 37 (2013) 2702–2708.
- [11] Y. Khan, A method for solving nonlinear time-dependent drainage model, *Neural Computing and Applications* 23 (2012) 411–415.
- [12] Y. Khan, M. Usman, Modified homotopy perturbation transform method: A paradigm for nonlinear boundary layer problems, *International Journal of Nonlinear Sciences and Numerical Simulation* 15 (2014) 19–25.
- [13] Y. Khan, K. Sayevand, M. Fardi, M. Ghasemi, A novel computing multi-parametric homotopy approach for system of linear and nonlinear fredholm integral equations, *Applied Mathematics and Computation* 249 (2014) 229–236.
- [14] Q. Mao, Application of adomian modified decomposition method to free vibration analysis of rotating beams, *Mathematical Problems in Engineering* 2013 (2013) 1–10.
- [15] J.-C. Hsu, H.-Y. Lai, C.-K. Chen, An innovative eigenvalue problem solver for free vibration of uniform timoshenko beams by using the adomian modified decomposition method, *Journal of Sound and Vibration* 325 (2009) 451–470.
- [16] H.-Y. Lai, C.-K. Chen, J.-C. Hsu, et al., Free vibration of non-uniform euler-bernoulli beams by the adomian modified decomposition method, *CMES–Comput. Model. Eng. Sci* 34 (2008) 87–116.
- [17] H.-Y. Lai, J.-C. Hsu, C.-K. Chen, An innovative eigenvalue problem solver for free vibration of euler–bernoulli beam by using the adomian decomposition method, *Computers & Mathematics with Applications* 56 (2008) 3204–3220.
- [18] Y. Khan, W. Al-Hayani, A nonlinear model arising in the buckling analysis and its new analytic approximate solution, *Zeitschrift für Naturforschung A* 68 (2013) 355–361.
- [19] H. Vázquez-Leal, Y. Khan, A. L. Herrera-May, U. Filobello-Nino, A. Sarmiento-Reyes, V. M. Jiménez-Fernández, D. Pereyra-Díaz, A. Perez-Sesma, R. Castaneda-Sheissa, A. Díaz-Sanchez, J. Huerta-Chua, Approximations for large deflection of a cantilever beam under a terminal follower force and nonlinear pendulum, *Mathematical Problems in Engineering* 2013 (2013) 1–12.
- [20] M. Akbarzade, Y. Khan, Dynamic model of large amplitude non-linear oscillations arising in the structural engineering: Analytical solutions, *Mathematical and Computer Modelling* 55 (2012) 480–489.
- [21] Y. Khan, M. Akbarzade, Dynamic analysis of nonlinear oscillator equation arising in double-sided driven clamped microbeam-based electromechanical resonator, *Zeitschrift für Naturforschung A* 67 (2012) 435–440.
- [22] D. Adair, M. Jaeger, Simulation of tapered rotating beams with centrifugal stiffening using the adomian decomposition method, *Applied Mathematical Modelling* 40 (2016) 3230–3241.
- [23] D. H. Hodges, M. J. Rutkowski, Free-vibration analysis of rotating beams by a variable-order finite-element method, *AIAA Journal* 19 (1981) 1459–1466.

- [24] S. Naguleswaran, Lateral vibration of a centrifugally tensioned uniform euler-bernoulli beam, *Journal of Sound and Vibration* 176 (1994) 613–624.
- [25] H. Yoo, S. Shin, Vibration analysis of rotating cantilever beams, *Journal of Sound and Vibration* 212 (1998) 807–828.
- [26] Free Vibration Analysis of Rotating Blades With Uniform Tapers, volume Design Engineering, Volumes 1 and 2 of *ASME International Mechanical Engineering Congress and Exposition*, 2003.
- [27] J. Banerjee, H. Su, D. Jackson, Free vibration of rotating tapered beams using the dynamic stiffness method, *Journal of Sound and Vibration* 298 (2006) 1034–1054.
- [28] Ö. Özdemir, M. Kaya, Flapwise bending vibration analysis of a rotating tapered cantilever bernoulli–euler beam by differential transform method, *Journal of Sound and Vibration* 289 (2006) 413–420.
- [29] S. M. Hashemi, M. J. Richard, Natural Frequencies of Rotating Uniform Beams with Coriolis Effects, *Journal of Vibration and Acoustics* 123 (2001) 444–455.
- [30] A. Kumar, R. Ganguli, Rotating Beams and Nonrotating Beams With Shared Eigenpair, *Journal of Applied Mechanics* 76 (2009) 051006.
- [31] R. J. Theodore, A. Ghosal, Comparison of the assumed modes and finite element models for flexible multilink manipulators, *The International Journal of Robotics Research* 14 (1995) 91–111.
- [32] A. De Luca, B. Siciliano, Closed-form dynamic model of planar multilink lightweight robots, *IEEE Transactions on Systems, Man, and Cybernetics* 21 (1991) 826–839.
- [33] F. Leckie, E. Pestel, Transfer-matrix fundamentals, *International Journal of Mechanical Sciences* 2 (1960) 137–167.
- [34] M. A. Dokainish, A New Approach for Plate Vibrations: Combination of Transfer Matrix and Finite-Element Technique, *Journal of Engineering for Industry* 94 (1972) 526–530.
- [35] V. H. Mucino, V. Pavelic, An exact condensation procedure for chain-like structures using a finite element-transfer matrix approach, *Journal of Mechanical Design* 103 (1981) 295–303.
- [36] B. Rong, X. Rui, G. Wang, Modified Finite Element Transfer Matrix Method for Eigenvalue Problem of Flexible Structures, *Journal of Applied Mechanics* 78 (2010) 021016.
- [37] T. Tan, A. Yousuff, L. Bahar, M. Konstantinidis, A modified finite element-transfer matrix for control design of space structures, *Computers & Structures* 36 (1990) 47–55.
- [38] R. W. Krauss, W. J. Book, Transfer Matrix Modeling of Systems With Noncollocated Feedback, *Journal of Dynamic Systems, Measurement, and Control* 132 (2010) 061301.
- [39] X. Rui, G. Wang, Y. Lu, L. Yun, Transfer matrix method for linear multibody system, *Multibody System Dynamics* 19 (2007) 179–207.
- [40] M. Sylla, B. Asseke, Dynamics of a rotating flexible and symmetric spacecraft using impedance matrix in terms of the flexible appendages cantilever modes, *Multibody System Dynamics* 19 (2008) 345–364.
- [41] N. Guy, D. Alazard, C. Cumer, C. Charbonnel, Dynamic modeling and analysis of spacecraft with variable tilt of flexible appendages, *Journal of Dynamic Systems, Measurement, and Control* 136 (2014).
- [42] D. Alazard, J. A. Perez, C. Cumer, T. Loquen, Two-input two-output port model for mechanical systems.
- [43] H. H. S. Murali, D. Alazard, L. Massotti, F. Ankersen, C. Toglia, Mechanical-attitude controller co-design of large flexible space structures, in: J. Bordeneuve-Guibé, A. Drouin, C. Roos (Eds.), *Advances in Aerospace Guidance, Navigation and Control*, Springer International Publishing, Cham, 2015, pp. 659–678.
- [44] J. A. Perez, D. Alazard, T. Loquen, C. Cumer, C. Pittet, Linear dynamic modeling of spacecraft with open-chain assembly of flexible bodies for ACS/structure co-design, in: *Advances in Aerospace Guidance, Navigation and Control*, Springer International Publishing, 2015, pp. 639–658.
- [45] J. A. Perez, D. Alazard, T. Loquen, C. Pittet, C. Cumer, Flexible multibody system linear modeling for control using component modes synthesis and double-port approach, *Journal of Dynamic Systems, Measurement, and Control* 138 (2016).
- [46] F. Sanfedino, D. Alazard, V. Pommier-Budinger, A. Falcoz, F. Boquet, Finite element based n-port model for preliminary design of multibody systems, *Journal of Sound and Vibration* 415 (2018) 128–146.
- [47] R. Rodrigues, V. Preda, F. Sanfedino, D. Alazard, Modeling, robust control synthesis and worst-case analysis for an on-orbit servicing mission with large flexible spacecraft, *Aerospace Science and Technology* 129 (2022) 107865.
- [48] R. Rodrigues, F. Sanfedino, D. Alazard, V. Preda, J. Olucha, Linear parameter-varying gain-scheduled attitude controller for an on-orbit servicing mission involving flexible large spacecraft and fuel sloshing, in: *ESA GNC and ICATT Conference 2023*, Sopot, Poland.
- [49] J. Chebbi, V. Dubanchet, J. A. Perez Gonzalez, D. Alazard, Linear dynamics of flexible multibody systems: A system-based approach, *Multibody System Dynamics* 41 (2017).
- [50] D. Alazard, F. Sanfedino, *Satellite dynamics toolbox library (sdtlib) - user’s guide*, 2021.
- [51] H. Murakami, O. Rios, T. J. Impelluso, A theoretical and numerical study of the dzhaniybekov and tennis racket phenomena, *Journal of Applied Mechanics* 83 (2016).
- [52] L. Meirovitch, Hybrid state equations of motion for flexible bodies in terms of quasi-coordinates, *Journal of Guidance Control and Dynamics* 14 (1991) 1008–1013.
- [53] H. Schaub, J. L. Junkins, *Analytical Mechanics of Space Systems*, Fourth Edition, American Institute of Aeronautics and Astronautics, Inc., 2018.
- [54] J. F. Hall, Problems encountered from the use (or misuse) of rayleigh damping, *Earthquake Engineering & Structural Dynamics* 35 (2006) 525–545.